Solar Energy 207 (2020) 270–288

Contents lists available at ScienceDirect

Solar Energy

journal homepage: www.elsevier.com/locate/solener

2-Terminal CIGS-perovskite tandem cells: A layer by layer exploration

T. Jesper Jacobsson[a,b,*], Adam Hultqvist[c,*], Sebastian Svanström[d], Lars Riekehr[c], Ute B. Cappel[e], Eva Unger[b,f], Håkan Rensmo[d], Erik M.J. Johansson[a], Marika Edoff[c], Gerrit Boschloo[a]

[a] Dept. of Chemistry – Ångström Laboratory, Uppsala University, Box 523, 75120 Uppsala, Sweden
[b] Young Investigator Group Hybrid Materials Formation and Scaling, Helmholtz-Zentrum Berlin für Materialen und Energie GmbH, Albert-Einstein Strasse 16, 12489 Berlin, Germany
[c] Dept. of Engineering Sciences, Solid State Electronics Division, Uppsala University, Box 534, 75121 Uppsala, Sweden
[d] Dept. of Physics and Astronomy, Uppsala University, Box 5516, 75120 Uppsala, Sweden
[e] Division of Applied Physical Chemistry, Dept. of Chemistry, KTH Royal Institute of Technology, SE-100 44 Stockholm, Sweden
[f] Chemical Physics and NanoLund, Lund University, P.O. Box 124, 22100 Lund, Sweden

ARTICLE INFO

Keywords:
Perovskite
CIGS
Tandem
2-terminal
Solar cell

ABSTRACT

This paper focuses on the development of 2-terminal CIGS-perovskite tandem solar cells by exploring a range of stack sequences and synthetic procedures for depositing the associated layers. In the end, we converged at a stack sequence composed of SLG/Mo/CIGS/CdS/i-ZnO/ZnO:Al/NiO/PTAA/Perovskite/LiF/PCBM/SnO_2/ITO. With this architecture, we reached performances only about 1% lower than the corresponding 4-terminal tandem cells, thus demonstrating functional interconnects between the two sub-cells while grown monolithically on top of each other. We go through the stack, layer-by-layer, discussing their deposition and the results, from which we can conclude what works, what does not work, and what potentially could work after additional modifications. The challenges for a successful 2-terminal tandem device include: how to deal with, or decrease, the surface roughness of the CIGS-stack, how to obtain uniform coverage of the layers between the CIGS and the perovskite while also obtaining a benign interface chemistry, and how to tune the band gaps of both the CIGS and the perovskite to obtain good optical matching. The investigation was based on CIGS with a power conversion efficiency around 14%, and perovskites with an efficiency around 12%, resulting in 2-terminal tandem cells with efficiencies of 15–16%. The results indicate that by using higher performing CIGS and perovskite sub-cells, it should be possible to manufacture highly efficient 2-terminal CIGS-perovskite tandem devices by using the protocols, principles, and procedures developed and discussed in this paper.

1. Introduction

Abundant supply of affordable energy is a fundament of our civilisation, and if we desire development and prosperity to continue to be hallmarks of our collective existence, we would better switch towards more long-term sustainable energy solutions. Photovoltaics could be an important part of that transition. Silicon technology is currently dominating the solar cell market, but there are contenders. Two of those, which are the focus of this paper, are solar cells based on lead halide perovskites and CIGS ($CuIn_xGa_{1-x}Se_2$), which if combined in a tandem architecture potentially could outperform standard single junction silicon.

Lead halide perovskite solar cells are the runner up in the PV-field (Correa-Baena et al., 2017). They entered the solar cell community as a nano-particle curiosity in 2009 (Kojima et al., 2009), and have since become a large research field including a variety of structures and material combinations and have now reached above 25% certified record efficiency (Green et al., 2019). This class of perovskites has a range of properties that has made this development possible. They are defect tolerant (Yin et al., 2014), have good transport properties, (Stranks et al., 2013; Herz, 2016; Herz, 2017) and long charge carrier lifetimes (Chouhan et al., 2017; de Quilettes et al., 2015). They also have a rich compositional complexity, enabling tunability of both band gap and other properties (Jacobsson et al., 2016b; Saliba, 2019). Lead halide perovskites are also reasonable simple to synthesise from solution in a standard lab environment, which has enabled fast feedback loops. Advancements in long-term stability, scalability, and reproducibility are still required, but given the recent pace of progress, the perovskites have a reasonable chance to end up as a low-cost, efficient, and competitive solar cell technology.

* Corresponding authors.
E-mail addresses: jacobsson.jesper.work@gmail.com (T.J. Jacobsson), adam.hultqvist@angstrom.uu.se (A. Hultqvist).

https://doi.org/10.1016/j.solener.2020.06.034
Received 10 February 2020; Received in revised form 26 May 2020; Accepted 7 June 2020
Available online 08 July 2020

In terms of efficiency for single junction technologies, silicon could probably be matched, but not outperformed, by perovskites. The same can be said about price. Silicon has the benefit of market dynamics, first mover advantage, and proven reliability. Perovskites with their tuneable band gap (Jacobsson et al., 2016b), their cheap precursor chemicals (Park et al., 2016), and the versatile set of synthetic pathways available (Saliba et al., 2018b), are, however, highly interesting for tandem architectures with the potential to go beyond and outperform single junction silicon (Bailie and McGehee, 2015; Almansouri et al., 2015). Perovskite tandem cells have consequently emerged as a hot topic, with work going on in CIGS-perovskite (Yang et al., 2015; Fu et al., 2017; Bailie et al., 2015; Guchhait et al., 2017; Shen et al., 2018; Han et al., 2018; Jost et al., 2019), silicon-perovskite (Mailoa et al., 2015; Albrecht et al., 2016; Duong et al., 2017; Raja et al., 2017; Werner et al., 2018a, 2018b; Quiroz et al., 2018; Zheng et al., 2018; Bush et al., 2018; Sahli et al., 2018b), and perovskite-perovskite tandem cells (Werner et al., 2018a; Eperon et al., 2016; Heo and Im, 2016; Rajagopal et al., 2017; Sheng et al., 2017). In this work we have exclusively focused on CIGS-perovskite tandem solar cells.

CIGS is a well-established thin film solar cell technology (Lee and Ebong, 2017), with record efficiency of 23.35 %[1] and a few percent of the commercial global PV-market. Despite the technological success, CIGS struggle in the competition with silicon. From the CIGS perspective, an interesting option would thus be to squeeze in a few extra production steps for depositing a perovskite top-cell for boosting the efficiency and thereby providing a competitive edge compared to standard silicon.

A tandem device is two separate solar cell technologies placed on top of each other dividing the solar spectrum between them and thereby lowering the overall thermalization losses. There is a certain degree of freedom in engineering contact structures and the current flow through such a device (Bailie and McGehee, 2015), where the most common distinction is between 4- and 2-terminal devices (Fig. 1a and b).

In the 4-terminal architecture, the two cells are independently wired. This has the advantage that the two sub-cells do not need to be current-matched and that they will be less sensitive with respect to spectral variations. They could also be developed, manufactured, and optimised independently. From an engineering perspective, this is probably the simpler approach, even though it requires additional transparent conducting oxide (TCO) layers, cables, and an additional maximum power point (MPP) -tracker. A handful of 4-terminal CIGS-perovskite cells have been reported in the literature (Yang et al., 2015; Fu et al., 2017; Bailie et al., 2015; Guchhait et al., 2017; Shen et al., 2018), several of which demonstrate efficiencies above 20% (Fu et al., 2017; Guchhait et al., 2017; Shen et al., 2018).

Conceptually, the 4-terminal architecture suffers from being two separate cells, needing two separate production lines joined by an assembly step in the end. The question whether they really should be a tandem at all will thus constantly loom over the device, as a geometrical transformation can turn them back into two separate solar cells that can be placed side-by-side. If they are, they will deliver considerably more power than they did in their tandem architecture. One of the cells will also, inevitable, perform better than the other, questioning the decision why not use two of the best cells instead. The reason behind the tandem integration is of course that geometrical footprint has a price in itself based on land use, encapsulation, wiring, etc. even though the performance window of economic advantage is narrow (Yu et al., 2018).

Two-terminal tandem cells on the other hand are monolithic units with series interconnected cells deposited on top of each other. This leads to a subtle change in the logic of the system, where the practical considerations narrow down to whether or not the tandem-cell performs better than the best of the individual cells, considering both performance and price. The industrial logic is also simple. Ideally, depositing the perovskite top-cell would only require a few extra production steps squeezed into the existing production line. The perovskite top-cell thus become an add-on, or a bonus, to something that already exists, be it silicon or CIGS.

The two-terminal cells also have some optical advantages, e.g. a reduction in the number of transparent conductive layers from three to two (T.2, T.3 and T.4 in Fig. 1a vs C.2 and T.2 in Fig. 1b), and the possibility of a thinner contact between the cells as no lateral conduction is required (C.2 in Fig. 1b compared to T.2 and T.3 in Fig. 1a). This potentially leads to less parasitic absorption and thereby to higher efficiencies.

The production of 2-terminal cells is, however, more challenging as the sub cells must be current matched, the bottom cell must be engineered to be a good substrate for top-cell deposition, and the top-cell deposition must not damage the bottom-cell. Based on the potential advantages, we have in this work focused on developing 2-terminal systems in spite of the higher technological and scientific challenges.

An existential question for a tandem device is if it in terms of efficiency can outperform its own two sub-technologies as well as silicon. The power output from 2-terminal devices depends on for example: the band gaps, quantum efficiencies, the V_{oc} loss for both sub-cells, the combined fill factor, the solar spectrum, and the spectral transmission of the top cell. An estimate of the maximum efficiency as a function of the two band gaps is given in Fig. 1c. The analysis is detailed in the SI and is based on AM 1.5G, perfect transmittance of the top-cells for sub band gap photon energies, a wavelength independent quantum efficiency of 0.9, a V_{oc} loss ($E_g - V_{oc}$) of 0.45 eV for the CIGS and 0.4 eV

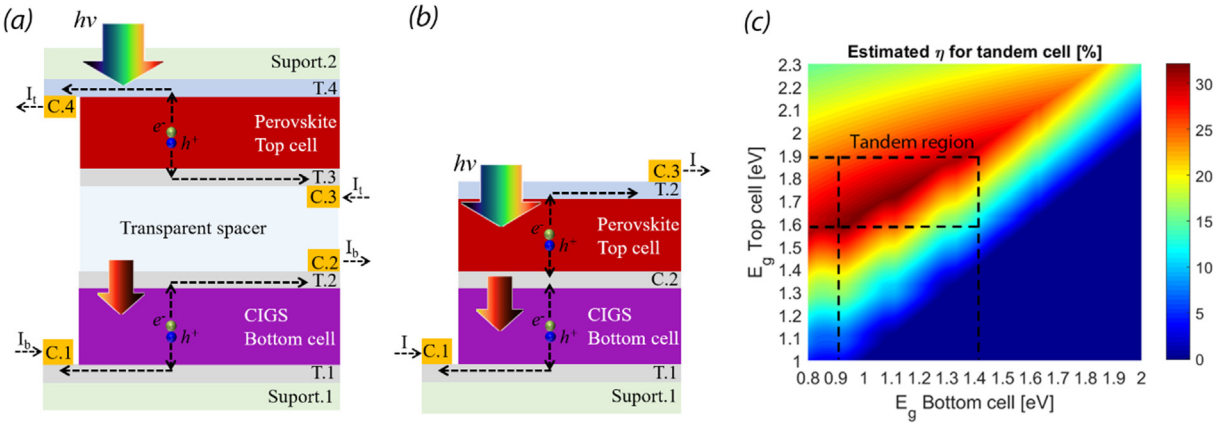

Fig. 1. (a) Schematics of a 4-terminal tandem cell with terminals (T) and contacts (C) indicated. (b) The architecture of a corresponding 2-terminal cell. (c) Estimate of maximum device performance of a CIGS-perovskite tandem cell, without surpassing current state-of-the-art for the CIGS and perovskite technology, given as a function of the two band gaps.

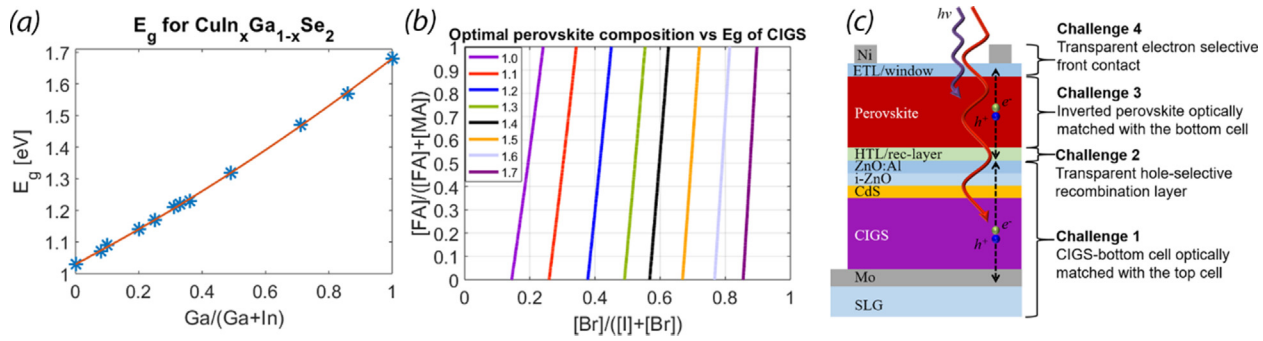

Fig. 2. (a) Band gap at room temperature of CIGS as a function of the In to Ga ratio. Data is adopted from Mudryi et al. (2010). (b) Optimal perovskite composition in the MA-FA-Pb-Br-I compositional space given for a number of possible CIGS band gaps. (c) An illustration of the main challenges with respect to the development of a CIGS-perovskite 2-terminal tandem device.

for the perovskite, and a combined fill factor of 0.75. The analysis shows that power conversion efficiencies (η) beyond 30% are realistically attainable without surpassing current state-of-the-art for individual perovskite and CIGS cells, given that the interface chemistry between all the layers in the device stack is optimized. More detailed simulations essentially result in the same upper bound (Almansouri et al., 2015; Filipič et al., 2015; Hörantner and Snaith, 2017; Futscher and Ehrler, 2017). This is sufficiently much higher than the performance of the individual cells that it may compensate for the additional production cost and the weather dependent fluctuation of the energy distribution of the solar spectra that temporarily may reduce the current matching.

One of the attractive features of CIGS-perovskite tandem cells is the tuneable band gaps. The band gap for CIGS at room temperature varies from 1.03 eV for $CuInSe_2$ to 1.68 eV for $CuGaSe_2$ Eq. (1) and Fig. 2a) (Mudryi et al., 2010), which includes the 1.34 eV ideal for a single band gap cell (Rühle, 2016; Shockley and Queisser, 1961), as well as what is needed for bottom-cells. In principle, CIGS could be used for both the top- and the bottom-cell. In practice, it has, however, been difficult to manufacture efficient high band gap CIGS, and the thermal budget of the bottom cell, i.e. max 200 °C for a few minutes, makes the deposition of a CIGS top-cell problematic. The perovskites complement the CIGS by not requiring high deposition temperatures and with a band gap that can be tuned between ~1.55 and 2.3 eV by changing the composition in terms of iodine to bromide content and FA to MA content Eq. (2). (Jacobsson et al., 2016b) For each possible CIGS band gap, there is thus a perovskite composition, extractable from Eq. (1) or Fig. 2b, that will give a perfect optical match.

$$E_g = 1.68x + 1.03(1-x) - 0.12x(1-x),\ x = Ga/(Ga+In) \quad (1)$$

$$E_g(x,y) = 1.58 + 0.436x - 0.0580y + 0.294x^2 + 0.0199x{\cdot}y$$
$$x = \frac{[Br]}{[Br]+[I]},\ y = \frac{[FA]}{[FA]+[MA]} \quad (2)$$

The challenges in constructing a 2-terminal CIGS-perovskite devices as schematically shown in Fig. 2c are numerous and include:

1) Deposition of an efficient CIGS-bottom cell which acts as a good substrate for subsequent perovskite deposition, and which has a band gap that provides current-matching with the perovskite top-cell.
2) Deposition of a recombination layer between the cells that does not damage the CIGS-stack, is transparent, is energetically aligned with nearby layers, act as a hole-selective contact with respect to the perovskite, and is a good substrate for perovskite deposition.
3) Deposition of a highly efficient, stable, perovskite in a p-i-n (inverted) structure, with a proper band gap and which is highly transparent in the sub band gap region.
4) Deposition of a transparent, electron selective top contact.

In this project, we have produced 2-terminal CIGS-perovskite tandem devices and explored the impact of various modifications in the stack sequence.

2. Experimental details

2.1. Preparation of tandem cells

2.1.1. Glass cleaning

Two different types of CIGS were produced, that here are labelled as smooth and rough. Low iron soda lime glass (SLG) was used as a substrate for the rough CIGS solar cell stack. For the smooth CIGS solar cell stack, a different float SLG with very similar properties was used. The glass substrates were cleaned following a previously established baseline procedure (Lindahl et al., 2013).

2.1.2. Mo deposition

The rough CIGS solar cell stack uses a bilayer of pulsed DC sputtered Mo, where the first thin layer is sputtered for adhesion and the second thicker layer is sputtered for conductivity. The thicker conductive layer follows the previously established baseline procedure (Lindahl et al., 2013), whereas the adhesion layer has since been added. During the adhesion layer sputtering the chamber pressure is increased to 15 mTorr and the effective sputtering time is reduced so that the resulting layer is 30 ± 10 nm thick. The smooth CIGS solar cell stack uses a Mo that is 280 ± 5 nm thick with a sheet resistance of 0.5 Ω/□ that behaves very similar to the Mo of the rough CIGS stack.

2.1.3. NaF

For the stack with the smooth CIGS, an 8 ± 2 nm thick NaF layer is evaporated onto the Mo prior to the CIGS deposition (Edoff et al., 2017). The layer acts as a Na source and is intentionally consumed during the subsequent CIGS co-evaporation

2.1.4. (A)CIGS deposition

The rough CIGS was co-evaporated using an inline baseline process (Lindahl et al., 2013) with film thickness of 1.5–2 μm and a linear bandgap profile with increasing bandgap from the top of the film to the Mo interface. Using the integrated peak areas from X-ray fluorescence, the average [Ga]/([Ga] + [In]) of the film was calculated to 0.44 ± 0.02 and the average [Cu]/([Ga] + [In]) was calculated to 0.88 ± 0.06.

A modified three stage process is used to co-evaporate the smooth CIGS films with a thickness of 2 ± 0.2 μm according to a previously developed procedure (Edoff et al., 2017). This process also intentionally replaces some Cu with Ag to the following extent [Ag]/([Ag] + [Cu]) = 0.2. The band gap is almost constant from the top of the film all the way through. However, at the interface towards the bottom, the band gap is intentionally increased to repel electrons away

from the CIGS/Mo interface [ACIGS]. From integrating the peak areas of the X-ray fluorescence of these films, the average ([Cu] + [Ag])/([Ga] + [In]) is 0.8 ± 0.1, whereas the average [Ga]/([Ga] + [In]) was intentionally varied in the range of 0.4–0.05 to investigate the effect of lower band gap CIGS.

2.1.5. CdS deposition

The CdS was deposited using a baseline chemical bath deposition (CBD) process (Lindahl et al., 2013), where Cd-acetate and thiourea are the chemical precursors for Cd and S respectively, and where ammonium hydroxide was added to drive the formation of CdS.

2.1.6. ZnO deposition

The i-ZnO layer was RF-sputtered according to the established baseline procedure (Lindahl et al., 2013), except that there was no oxygen gas present during the presputtering stage. Similarly, the ZnO:Al sputtering also mostly followed the baseline procedure (Lindahl et al., 2013), but was RF-sputtered at 400 W for 125 s. Unless stated otherwise, this resulting in a thickness of 230 ± 20 nm and a sheet resistance of 50 ± 5 Ω/□ as measured on glass.

2.1.7. NiO deposition

NiO films were deposited by reactive pulsed DC sputtering at 500 W from a metallic Ni target. The gas flows into the chamber were 25 sccm of O_2 and 25 sccm of Ar and the resulting pressure was regulated to 6 mTorr. Unless specified otherwise, the deposition time was 45 s which result in a 25 ± 5 nm thick film as measured by a profilometer and cross section SEM.

2.1.8. PTAA deposition

PTAA was dissolved in toluene at 2 mg/ml. The substrates with NiO was inserted into a nitrogen filled glove box where the PTAA was spin coated on the substrates. 50 µl PTAA solution was dynamically spin-coated at 4000 rpm for 30 s. The samples were then placed on a hotplate at 100 °C for 10 min, where after they were cooled down to room temperature within the glove box. The perovskite was spin coated directly after PTAA deposition (i.e. 5–45 min) within the same glovebox.

2.1.9. Perovskite deposition

Perovskite precursor solutions were prepared in a glovebox with an argon atmosphere. In the base procedure, stock solutions of PbI_2 and $PbBr_2$ were prepared in advance, whereas the final precursor solutions were prepared just before perovskite deposition. Anhydrous DMF:DMSO in the proportion 4:1 was used as solvent. The PbI_2 and $PbBr_2$ solutions are close to the saturation point, and to ensure that the lead salts are complete dissolved, the solutions were heated under steering at a hotplate at approximately 100 °C for 20 min, and then cooled down to room temperature just before use. In the standard case, two master solutions were prepared, (a) 1.35 M PbI_2 and 1.24 M FAI, (b) 1.35 M $PbBr_2$ and 1.24 M MABr. Those were mixed in the proportion a:b = 83:17, which gives the standard perovskite $FA_{0.83}M_{0.17}PbBr_{0.51}I_{2.49}$. For Cs and/or Rb doping, two additional solutions were prepared: 1.38 M CsI in DMSO and 1.38 M RbI in DMSO. Those solutions were prepared in advance. In the standard case, a volume corresponding of each of those solutions corresponding to 5% of the volume of the perovskite solution were added to the final precursor solution.

The MA and FA salts were bought from Dyesol, the lead salts from TCI, solvents from Fisher, and the remaining chemicals from Sigma Aldrich. All chemicals were used as received without further treatment.

During the cause of the project, a number of slightly different perovskite mixtures were used, as indicated in the supplementary file with data for all devices made. Compare to the baseline case described here, the variations used are listed as follows, where the perovskite label refers to the key in the supplementary file.

- M_Cs: The two master solutions were slightly more diluted with concentrations of (a) 1.25 M PbI_2 and 1.14 M FAI, (b) 1.25 M $PbBr_2$ and 1.14 M MABr. 5 vol% addition of 1.38 M CsI in DMSO. No addition of Rb.
- M_Cs_3: 5 vol% addition of 1.38 M CsI in DMSO. No addition of Rb.
- M_Cs_Rb: The two master solutions were slightly more diluted with concentrations of (a) 1.25 M PbI_2 and 1.14 M FAI, (b) 1.25 M $PbBr_2$ and 1.14 M MABr. 5 vol% addition of 1.38 M CsI in DMSO and 4% addition of 1.38 M RbI in DMSO.
- M_Cs_Rb_6: As described in the baseline procedure.
- M_Cs_Rb_7: A perovskite with a slightly higher band gap. The two maser solutions, (a) 1.35 M PbI_2 and 1.24 M FAI, (b) 1.35 M $PbBr_2$ and 1.24 M MABr where mixed in the proportion 77:23.
- M_Cs_Rb_8. A perovskite with a higher band gap. Four master solutions were prepared: (a) 1.35 M PbI_2 and 1.24 M FAI, (b) 1.35 M $PbBr_2$ and 1.24 M MABr, (c) 1.35 M PbI_2 and 1.24 M MAI, (d) 1.35 M $PbBr_2$ and 1.24 M FABr. The solutions were mixed in the proportions: a:b:c:d = 36.9 : 14.9 : 18.2 : 30.2. That gives a perovskite with FA:MA = 67:33 and I:Br = 55:45. 5 vol% addition of 1.38 M CsI in DMSO and 4% addition of 1.38 M RbI in DMSO
- M_Cs_Rb_9: A perovskite with a higher band gap. The same solutions as for M_Cs_Rb_8 were used. Those were mixed in the proportion a:b:c:d = 46.5:9.5:15.5:28.5. That gives a perovskite with FA:MA = 75:25 and I:Br = 62:38. 5 vol% addition of 1.38 M CsI in DMSO and 4% addition of 1.38 M RbI in DMSO
- CsFAPbBrI_2: A stoichiometric MA-free perovskite. A bit trickier to do due to lower solubility of CsI. Three master solutions where prepared: (a) 0.9 M PbI_2 and 0.9 M FAI, (b) 0.9 M $PbBr_2$ and 0.9 M MABr, (c) 0.9 M PbI_2 and 0.9 M CsI. Those were mixed in the proportion a:b:c = 66:17:17. The CsI does not dissolve properly wherefore solution (a) and (b) where poured into (c) in the right proportion.

The perovskites were spin-coated in a nitrogen-filled glove box. For each sample with a dimension of 1.4 * 2.4 cm, 35 µl precursor solution was spread over the substrate, which thereafter was spin-coated using a two-step program. The first step was a spreading step using a rotation speed of 1000 rpm with an acceleration of 200 rpm/s for 10 s. That step was immediately, without pause, followed by the second step where the films were spun at 6000 rpm for 30 s using an acceleration of 2000 rmp/s. During the second step, when approximately 10 s of the program remains, 100 µl of anhydrous chlorobenzene was applied on the spinning film with a hand-held automatic pipette. This last step, known as the antisolvent method, has a large impact on film morphology and result in significantly better device performance (Zhao and Zhu, 2014; Xiao et al., 2014; Jeon et al., 2014). This is the base procedure which were used unless something else is stated. For some samples, different spin-coating parameters were used, but when so were done it is stated in the supporting file specifying the synthetic procedure and results for all devices.

Directly after spin-coating, the films were placed on a hotplate at 100 °C where they were annealed for 30–70 min. After annealing, the samples were cooled to ambient temperature within the glove box. For samples with spin-coated PCBM, the PCBM were at this stage spin-coated in the same glove box.

After perovskite deposition, or after PCBM spin-coating, the samples were stored in air in a desiccator until further processing.

2.1.10. PCBM deposition by spin-coating

PCBM-60 was bought from Solenne. The PCBM was dissolved in chlorobenzene in an argon filled glovebox. The PCBM concentrations used were 0.2, 1, 2.5, 5, 10, 20, and 40 mg/ml. The PCBM solution were dynamically spin-coated on the perovskite at 4000 rpm for 20 s.

2.1.11. LiF, C60, and PCBM evaporation

The LiF, the C60, and the PCBM 60 were thermally evaporated from

a tungsten boat in an evaporator from Leica (EM MED020) at a pressure of around $2 \cdot 10^{-5}$ Torr. The evaporator is placed in normal lab environment meaning that samples will be exposed to air before evaporation.

LiF was deposited as a 1 nm thick film, as measured by the evaporators internal QCM. LiF was in the form of a powder and care hade to be taken while evaporating it. If the temperature of the tungsten boat is increased to fast, the powder in the bottom of the boat will heat up before the rest which could lead to the spread out of large burst of powder. We thus aimed at slow heating of the tungsten boat and a slow evaporation rate, i.e. 0.1 Å/s or less.

C60 was bought from Solenne. It was deposited with a thickness of 25 nm at an evaporation rate around 0.1 Å/s. When C60 was evaporated on top of LiF, the vacuum of the evaporator had to be broken in order to change the evaporation boat, which means that the samples were exposed to air between evaporations.

The PCBM was evaporated in the same way as C60. The thickness of the PCBM layer was 10 nm in all cases except one where it was 30 nm.

A so far not fully supported hypothesis is that evaporation speed is more important for PCBM than for C60, and that a lower evaporation speed of PCBM is significantly better than a faster one. At a lower evaporation rate, i.e. lower temperature, the PCBM left in the tungsten boat after evaporation have a compact, black, and shiny appearance, whereas at a higher evaporation speed, i.e. higher temperature, it gets a fluffier, mat, sponge-like texture.

After evaporation, the samples were stored in air in a desiccator until further processing.

2.1.12. ITO deposition

The ITO layers are deposited by RF-sputtering of a compound ITO target at 660 W for 120 s, unless stated otherwise. This results in a 240 ± 10 nm thick film and a sheet resistance of 55 ± 5 Ω/□ when deposited on glass. The gas flow into the chamber consisted of 1.6 sccm O_2 and 40 sccm Ar and the total pressure was regulated to be 6 mTorr.

2.1.13. Defining cell geometry

For the tandem cells. In the first 9 batches, the cell area was around 0.12 cm^2, defined by scribing done by hand. This gave 18 individual cells per substrate (9 if divided into two). In batch number 10, the cells were 0.0961 cm^2 and defined by machine scribing. In the remaining five batches, the cell area was 0.05 cm^2 and given by machine scribing. This gave 50 cells per substrate (20 if they were split into two). For the semitransparent single junction perovskite cells, the cell geometry was the same.

For opaque single junction perovskite cells, no subdivision of the substrate was done thus leaving one cell per substrate. During IV-measurements of those cells, a metal mask was used to limit the active cell area to 0.126 cm^2.

2.2. Deposition of perovskite p-i-n control cells

For XRD, UV–Vis, and fluorescence measurements, the perovskites were deposited on soda lime glass (SLG). For solar cell fabrications, FTO substrates were used. The FTO substrates were cleaned using helmanex and a tooth brush, and thereafter ultra-sonicated for 30 min in a helmanex bath, followed by an ethanol bath, followed by an acetone bath.

On top of the FTL, a NiO layer was sputtered in the same way as for the tandem cells described above. The FTO/NiO substrates where stored in air until introduced into the nitrogen filled glove box prior to perovskite deposition.

The perovskite deposition procedure was the same as for the tandem devices described above.

The ETL in the form of spin-coated PCBM, evaporated LiF, C60, PCBM, or SnO_2 by ALD was done in the same way as described for the tandem cells.

As a front contact, either ZnO:Al or a metal, i.e. Au or Ag was used. The ZnO:Al was deposited in the same way as for the tandem cells. The metal contacts were deposited by thermal evaporation at a pressure of $2 \cdot 10^{-5}$ Torr to a thickness of 80–100 nm.

2.3. Deposition of perovskite n-i-p control cells

The FTO substrates were prepared as described for deposition of p-i-n control cells.

A hole blocking layer of TiO_2 was deposited on the cleaned FTO substrates using spray pyrolysis. The spray solution was composed of ethanol, acetyl acetone, and titanium diisopropoxide (30% in isopropanol) in the proportions 90:4:6 by volume. Oxygen at a base pressure of 1 bar was used as a carrier gas. The glass substrates were heated to 450 °C on a hotplate and kept at that temperature for 15 min prior to the spraying. After an additional 30 min at 450 °C, the sprayed glass substrates were slowly cooled to room temperature. 10 ml of spray solution was used to cover 200 cm^2 of substrates. This procedure gives a compact layer of anatase with a thickness of around 20–30 nm.

On top of the compact TiO_2-layer deposited by spray pyrolysis, a mesoporous scaffold of TiO_2 nanoparticles was spin-coated. TiO_2 paste (30 NR-D) was bought from Dyesol and was dissolved in ethanol at a concentration of 150 mg/ml. On each substrate (1.4·1.4 cm), 50 µl of the TiO_2 solution was applied and spin-coated at 4000 rpm, with an acceleration of 2000 rpm/s, for 10 s. A piece of scotch tape was used on one side of the substrates to prevent the mesoporous TiO_2 to form where the front contacts were to be deposit. The substrates with mesoporous TiO_2 were sintered at 450 °C in air on a hot plate for 30 min and then slowly cooled to ambient temperature.

Prior to perovskite deposition, the substrates with mesoporous TiO_2 underwent a lithium treatment which has been found to be beneficial for the device performance (Giordano et al., 2016). On the substrates, 100 µl of a 35 mM Lithium bistrifluoromethanesulfonimidate (Li-TFSI) in acetonitrile was applied and spun at 3000 rpm for 10 s. The substrates were then thermally annealed in air at 450 °C for 30 min and then slowly cooled to 150 °C where after they were brought directly into a glovebox for perovskites deposition.

The perovskite deposition was done in the same way as when deposited on tandem devices described above.

After annealing of the perovskite films, a solid-state hole-conductor was spin-coated on top of the films in the same glove box. A 70 mM solution of Spiro-MeOTAD (spiro) dissolved in chlorobenzene was used as a hole conductor. To improve the performance of the spiro, three different additives were added: (Abate et al., 2013, 2014) 4-*tert*-butylpyridine, 1.8 M Li-TFSI in acetonitrile, and 0.25 M Co[t-BuPyPz]$_3$[TFSI]$_3$, also known as FK209, in acetonitrile. The Spiro:FK209:Li-TFSI:TBP molar ratio was 1:0.05:0.5:3.3. The spiro solution was prepared on the same day as the perovskite films were deposited.

The spiro was deposited by spin-coating at 4000 rpm for 20 s. 50 µl of the solution was deposited on the spinning film, using a hand-held automatic pipet, a few seconds into the spinning program. The samples were stored in a desiccator with silica gel.

Before the back contact was deposited, the perovskite/spiro layer was removed from one end of the samples using a razorblade, acetonitrile, and a cotton bud. An 80 nm thick gold back contact was deposited by vapour deposition at a pressure of around $2 \cdot 10^{-5}$ Torr.

2.4. Characterisation

2.4.1. IV-measurements of tandem cells

The JV of the top, bottom and tandem solar cells were measured with a Newport ABA solar simulator, where the light intensity was calibrated using a Hamamatsu S1337-66BR silicon photodiode to give the same short circuit current density in the solar simulator as the photodiode has under AM 1.5 illumination. Unless stated otherwise, the sweep is performed from positive to negative bias at 400 mV/s.

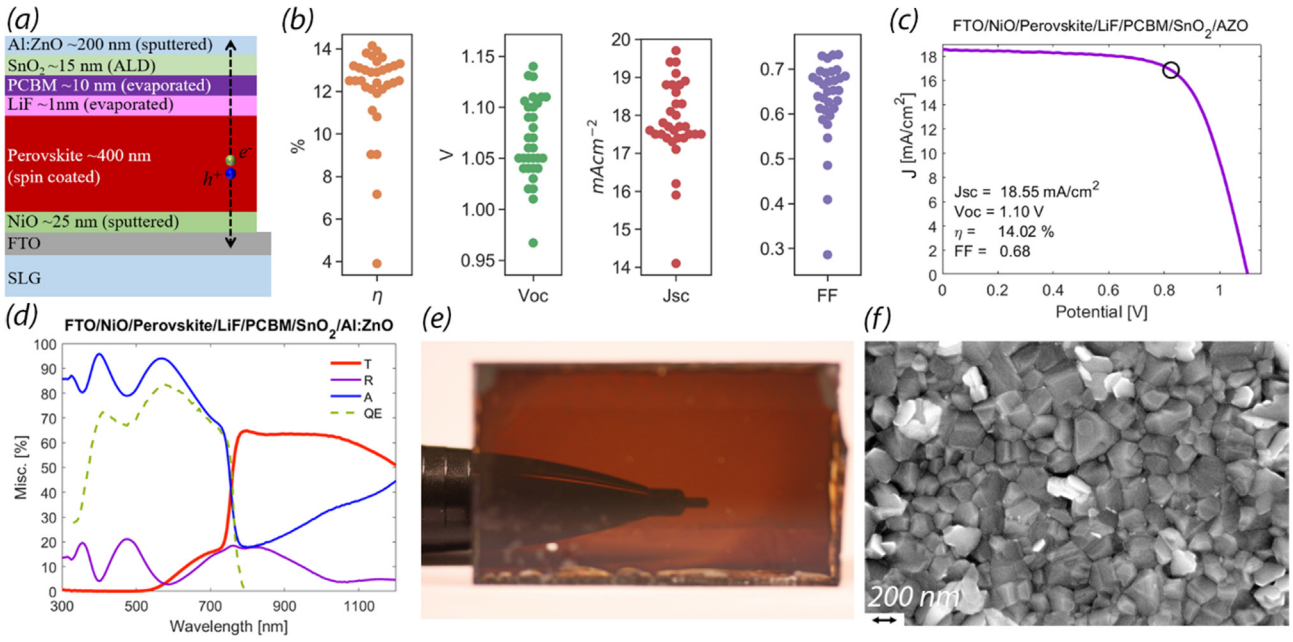

Fig. 3. (a) Sketch of the device stack of the semi-transparent pin-perovskite cells. (b) Spread of device performance of cells with the device stack in (a). (c) JV-data for the champion semi-transparent p-i-n device with NiO as an HTL. (d) Optical characterisation of a representative FTO/NiO/perovskite/PCBM/SnO_2/i-ZnO/ZnO:Al device. (e) A photo illustrating the transparency of the device. (f) Top view SEM of the perovskite deposited on FTO/NiO.

2.4.2. QE measurements

The external quantum efficiency is measured for bottom and top-cells using a homebuilt setup. The setup employs a Newport Oriel Apex monochromator, a signal chopper, a beam splitter with a reference cell, a pre-amplifier SRS SR570 for the device under test signal and two lock in amplifiers, SRS SR810 and SRS SR830.

2.4.3. Optical characterisation

Optical transmission and reflectance are measured with a Bentham PVE300 system using a monochromator and an integrating sphere. The investigated interval of wavelengths was 300–1200 nm with a measurement point either every 2 nm or every 5 nm.

2.4.4. UV–vis

UV–vis absorption measurements were performed on an Ocean Optics spectrophotometer HR-2000 c with deuterium and halogen lamps. In all measurements, a full spectrum from 190 to 1100 nm with 2048 evenly distributed points was sampled.

2.4.5. SEM

SEM imaging was carried out using a Zeiss LEO 1550 scanning electron microscope.

2.4.6. IV of control cells

Control cells with non-transparent metal front contacts were illuminated from the FTO side. The IV-characteristics of the devices were measured using a home-built system. To simulate solar light, a Newport solar simulator (model 91160) with a xenon arc lamp and an AM 1.5 filter was used. The light intensity was calibrated to 100 mW/cm^2 with a silicon photodiode. The IV-curves were measured with a digital source meter (Keithley 2400). No equilibration time or light soaking was applied before the potential scan. The starting point for the measurements was chosen as Voc plus ~0.05 V. From that point, the potential was scanned to short circuit and back again using a scan speed of 20 mV/s. Thereafter, the dark current was sampled using the same scan speed. The cells were masked with a metal mask in order to limit the active cell area to 0.126 cm^2.

2.4.7. TEM

To investigate the various interfaces and their chemistry, scanning transmission electron microscopy (STEM) and elemental mapping with energy dispersive X-ray spectroscopy (STEM-EDX) was used. Cross-section samples were prepared with a focused ion beam and scanning electron microscope (FIB-SEM, FEI Strata DB235) and attached to a Ti support grid using an in-situ lift out technique. The samples were then thinned to electron transparency with a final polishing step using 5 kV Ga ions. The STEM measurement was carried out on a probe corrected FEI Titan Themis operated at 200 kV and equipped the SuperX system for EDX analysis. The EDX data was acquired and evaluated with the software ESPRIT 1.9 from Bruker.

3. Results and discussion

3.1. Concerning the perovskite top cell

Our laboratory's baseline perovskite procedure is based on our previous works (Jacobsson et al., 2016a, 2016b, 2018), and results in n-i-p cells with FTO/TiO_2/TiO_2-mp/perovskite/Spiro/Au. During the timeframe of this project, the efficiency, determined from IV-scans, of our control cells were around 16–17%, with peak performance around 19%. See SI for details.

Many of the best performing perovskites today have a composition comparable to $Cs_{0.05}FA_{0.79}MA_{0.16}PbBr_{0.49}I_{2.51}$, doped with Rb and with a surplus of PbI_2 (Correa-Baena et al., 2017; Saliba et al., 2016a, 2016b; Bella et al., 2018). In most of our experiments, we used either this or similar compositions. The band gap of this composition is around 1.66 eV (Jacobsson et al., 2016b) (SI), which is on the low energy side in the tandem region shown in Fig. 1c. The band gap can be increased by increasing the amount of Br, but there is a trade-off as a Br ratio in excess of 40–50% often results in a phase instability with a reversible, possibly light induced, separation into I and Br richer regions that are detrimental for device performance (Jacobsson et al., 2016b; Unger et al., 2017). Whether such high band gap perovskites can be fully stabilised is still an open question, but with the use of a low band gap CIGS, it should be possible to us a perovskite material within the perovskite region of demonstrated relative compositional stability.

Given the device stack of the CIGS-cell, the standard n-i-p perovskite stack must be changed to the inverted p-i-n configuration, which leads to a set of new challenges. Before tackling the full problem of a tandem integrated top-cell, we developed protocols for semi-transparent inverted top cells deposited on FTO. During the course of this project, we performed a large number of tests with different hole-transport layers, electron-selective contacts, and contact structures, which for conciseness not will be described here but in another paper. The core results is that we ended up with the device stack in Fig. 3a composed of: FTO/NiO (15–20 nm, sputtered)/Perovskite (Cs and/or Rb mixed FA-MAPbBrI)/LiF (1 nm, evaporated)/PCBM (10 nm, evaporated)/SnO_2 (10 nm, ALD)/TCO (sputtered i-ZnO/ZnO:Al). Devices with this configuration showed rather consistent results (Fig. 3b) with average values of η = 12%, Voc = 1.07 V, Jsc = 17.8 mA/cm^2, and FF = 0.63. The best cell was around 14.5% efficient and the IV data for that cell is shown in Fig. 3c. The optical transmission of the same device is given in Fig. 3d, and illustrated in the photo in Fig. 3e. A top view SEM image of the perovskite deposited on NiO is given in Fig. 3f. The hysteresis during IV measurements was for the semi-transparent cells similar to the one for opaque nip control cells (see Fig. SI.3b for a typical example), i.e. noticeable nut not larger than what is normal for cells in this efficiency range. We did, however, noticed that cells with NiO HTL sometimes required a short period of illumination before they worked properly, i.e. the first recorded IV-curve sometimes looked different from subsequent consecutive IV-scans.

Based on the literature, there is room for an additional 5–7% unit increase in performance for the semi-transparent perovskite top cell (He et al., 2018; Hu et al., 2017; Xie et al., 2017; Wu et al., 2017; Chen et al., 2017; Bai et al., 2017; Xue et al., 2017; Chen et al., 2016). Although a 14% efficient top cell with a transparency around 70% will not give record tandem devices, it is a good starting point for exploring the impact of surrounding layers and interfaces and for further 2-terminal tandem cell development.

3.2. Concerning the CIGS bottom cell

35 CIGS bottom cells with a standard stack of SLG/Mo/CIGS/CdS/i-ZnO/Al:ZnO (Fig. 4a) were used for producing around 200 tandem samples, each with about 50 individual cells. These CIGS cells were produced in two different experimental setups that for reasons still under exploration produce CIGS with slightly different properties, e.g. surface roughness. To distinguish between those samples, they are labelled as either smooth or rough.

The best performing CIGS-cells tend to have a band gap around 1.2 eV. That value is right within the tandem region as defined in Fig. 2c. In practice, a lower band gap would be advantageous as the perovskite top-cell not will be perfectly transparent. It also seems advantageous to be in the lower energy side of the tandem region as the best perovskite cells to date have a band gap around 1.6 eV. During initial prototyping, we used rough CIGS solar cells with a band gap between 1.15 and 1.2 eV, whereas we later aimed for smoother CIGS with a lower band gap, i.e. 1.0–1.12 eV. Lowering the band gap unfortunately decreased the cell performance (Fig. 4c). Looking at all CIGS cells used, with different band gaps and surface roughness, the top performance was: η = 16%, Voc = 0.7 V, Jsc = 34.8 mA/cm^2, and FF = 0.75. The average performance for the smooth CIGS was: η = 12.8%, Voc = 0.55 V, Jsc = 33.2 mA/cm^2, FF = 0.69, and for the rough CIGS: η = 11.3%, Voc = 0.63 V, Jsc = 27.2 mA/cm^2, FF = 0.60 (Fig. 4b, d, e and SI).

In an ideal situation, the standard CIGS-stack could be used directly as a substrate for the perovskite top cell. For a scalable industrially feasible process, that is probably necessary. Unfortunately, there are complicating factors where surface roughness and morphology are particularly worrisome and thus must be controlled. The surface roughness can under standard CIGS deposition conditions be as high as a few hundred nm (Jehl et al., 2012), which is in the same order as the thickness of the subsequent perovskite solar cell layers. A non-uniform substrate means that subsequent layers deposited by wet chemical techniques, e.g. spin-coating, will not be of uniform thickness. This in turn leads to difficulties in depositing a uniform and fully covering hole selective contact, which means that the perovskite may be in direct contact with the mid-TCO and thereby opening up efficient recombination pathways. An example of a rough CIGS-surface that worked fine in the standard CIGS-stack but considerably less so in our tandem architecture is given in Fig. 4h. The roughness must be dealt with, and there are basically three available approaches.

One approach that was demonstrated by Han et al. (2018) involves depositing a thick ITO layer on top of the CIGS-stack, and mechanically polished down the ITO to flatness before subsequent perovskite deposition. The method worked, and they accomplished 2-terminal tandem cells with efficiencies above 20%. This method will, however, probably be hard to scale up commercially.

Another approach is to utilise vapour deposition techniques also for the top cell as demonstrated by Jost et al. (2019) To prevent shunts between the TCO and the perovskite, they utilised ALD for depositing a NiO HTL with conformal surface covering, which together with a thin PTAA layer enabled them to also demonstrate 2-terminal devices with efficiencies above 20% (Jost et al., 2019). If the surface roughness of the CIGS is in the same order as the thickness of the perovskite layer, i.e. ~400 nm, the problem may, however, remain and propagate up through the stack. Hills, ridges, and other convex protrusions at the surface pose a problem when depositing the perovskite films as these vertical structures may penetrate the perovskite film and cause shunts. That is unless every layer is deposited with vapour technologies. Even then, unless ALD is used, nooks and crannies at the surface can block the line of sight from the evaporation sources whereupon voids and pinholes can form. In terms of performance, vapour deposited perovskites have lagged behind their spin-coated counterparts. Vapour deposition is also less flexible in terms of the compositional engineering necessary for band gap tuning as that requires the simultaneous use of multiple evaporation sources; at least that has been the case for perovskite deposition over the last ten years. To our knowledge, no results have been published yet on 2-terminal CIGS-perovskite tandem cells with evaporated perovskites. That is, however, probably only a question of time, especially given the resent results on evaporated perovskites for silicon-perovskite tandem cells on textured silicon surfaces (Werner et al., 2018a; Sahli et al., 2018a).

A third approach to the surface roughness problem is to engineer the CIGS-deposition in such a way that a smoother CIGS is formed, and thereby to some extent avoid the problem altogether. We have produced CIGS in two different experimental setups, which give CIGS with different surface roughness. Typical examples of a smoother and a rougher CIGS are given in Fig. 4f–i. Deposition of CIGS with less surface roughness is possible, and the difference in surface roughness appears to only have a small effect on the CIGS performance (Fig. 4b). It does, however, have a clear impact on the tandem cell performance, especially in terms of performance homogeneity, which is superior when using the smoother CIGS, which we have seen here.

3.3. The four-terminal analogue

The goal of the project is the development of 2-terminal tandem devices, but for benchmarking purposes, the corresponding equivalent 4-terminal performances were investigated as well. This was done by measuring representative standalone perovskite and CIGS-cells, as well as CIGS-cells filtered by the semi-transparent perovskite top-cell (Table 1 and Fig. 5a and b) with an air gap of a few mm in between.

The bottom CIGS-cells lose about two thirds of their J_{sc} when the light is filtered through the perovskite-top cell (Fig. 5a). That is more than expected given the analysis based on realistic best case senarios (Fig. 1c), and is due to non-ideal transmission of the perovskite, the extra TCO layers, and the FTO substrate (Fig. 5b). Based on the quality

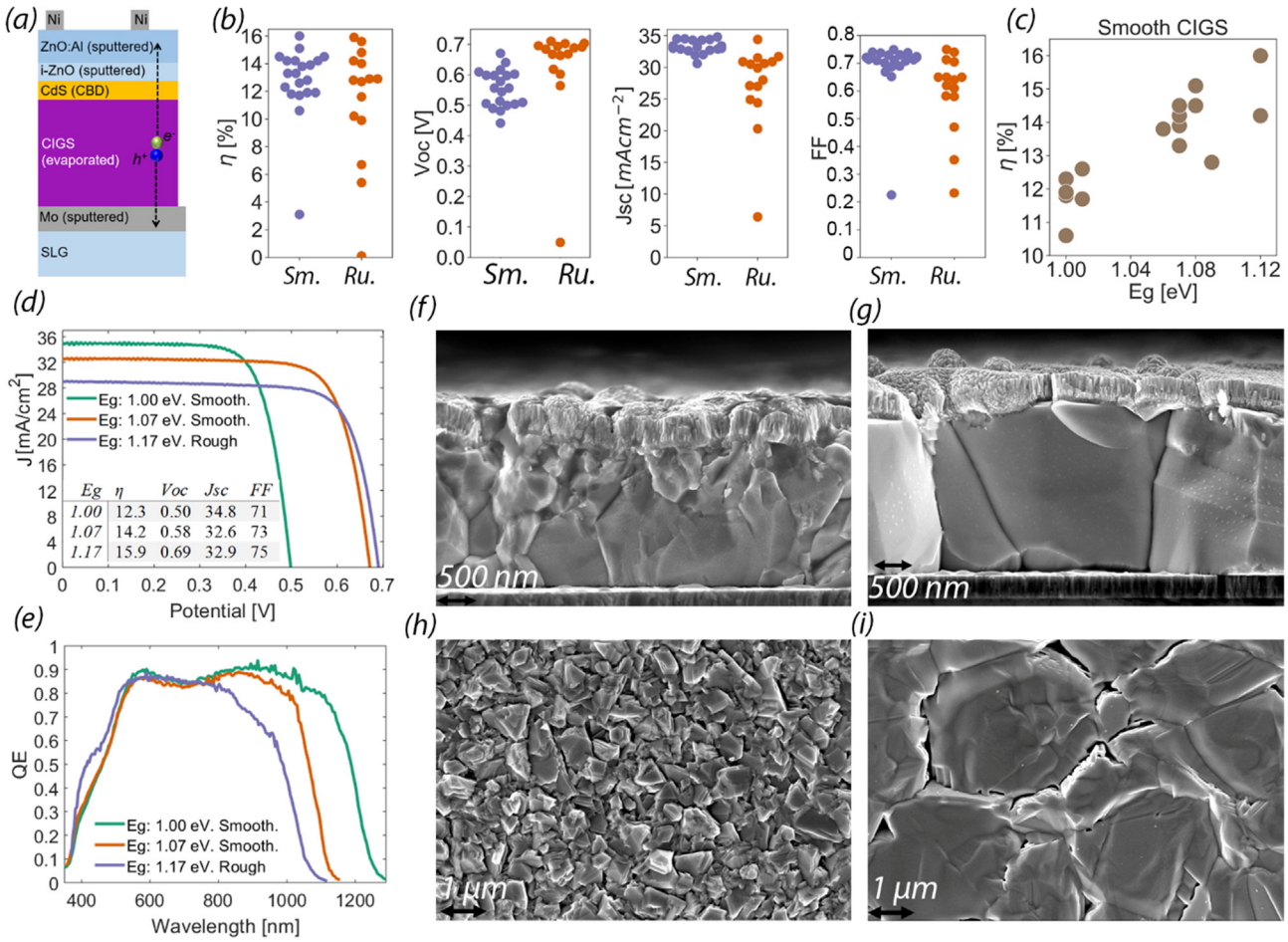

Fig. 4. (a) Standard CIGS stack. (b) Performance parameters for the full set of CIGS cells used for tandem integration in this project. Data is separated by experimental setup and marked as smooth (Sm.) and rough (Ru.) as described in the text. (c) Efficiency vs band gap for the set of smoother CIGS. (d) JV-data for a representative CIGS-cell. (e) QE-data for the cells in (d). (f and g) SEM cross section for full stack based on (f) more rough CIGS and (g) smoother CIGS. (h and i) SEM top view of (h) more rough CIGS and (i) smoother CIGS.

of the perovskite and its asociated absorption profile (Fig. 5b), a better optical match that partly compensates for the poor transission would be possible by decreasing the CIGS band gap. That is also in line with our observations where CIGS with a slighly lower band gap under perovskite filtration performes better than CIGS with a slighly higher band gap (Fig. 5a), despite them being equaly good under AM 1.5. For a 2-terminal cell, this will be even more important.

A CIGS-cell in a tandem configuration will only receive a part of the incoming light, and will be completely deprived of UV-photons. It has been argued that blue light is important for CIGS performance due to filling of trapps (Lany and Zunger, 2006; Siebentritt et al., 2010), and in our filtered cells we observed a slight decrease in Voc, FF, as well as in the internal QE, in line with that reasoning. On the other hand, much of the performance decrease in the filtered cells can be explained by absorption losses, and other recent results demonstrate good performance for filtered CIGS bottom cells (Guchhait et al., 2017; Shen et al., 2018). All things considered, top-cell absorption does not appear to be a significant problem for CIGS-perovskite cells.

A 16% efficient CIGS cell combined with a 12% efficient perovskite cell will not result in record devices in a 4-terminal configuration, and we reached around 17% (Table 1). This provide a target to aim for while constructing actual 2-terminal devices, and if the 2-terminal devices can approach this efficiency, that will be a demonstration of an electronically functional tandem stack.

3.4. Towards a 2-terminal CIGS-perovskite tandem design. Layer by layer

During the cause of the project, a total of 169 2-terminal CIGS-perovskite tandem samples were assembled, each with up to 50 individual cells. After initial prototyping (see SI for further details), we settled for the device layout in Fig. 6a with 2.4 · 1.4 cm substrates on which 50 individual cells were machine scribed with an individual

Table 1
4-terminal tandem cell performance. Smooth CIGS with two different band gaps where used together with a semi-transparent perovskite top cell (FTO/NiO/Perovskite/LiF/PCBM/SnO_2/Al:ZnO).

Cell	Eg [eV]	Voc [V]	Jsc [mA/cm^2]	FF [%]	η [%]	4-terminal η [%]
Perovskite top cell	1.66	1.04	17.5	65.2	11.9	–
CIGS-1 bottom-cell	1.08	0.64	34.0	75.2	16.4	–
CIGS-1 filtered by the top cell	1.08 (1.66)	0.60	11.8	74.2	5.3	17.2
CIGS-2 bottom-cell	1.12	0.68	31.9	76.7	16.5	–
CIGS-2 filtered by the top cell	1.12 (1.66)	0.64	10.6	69.5	4.7	16.6

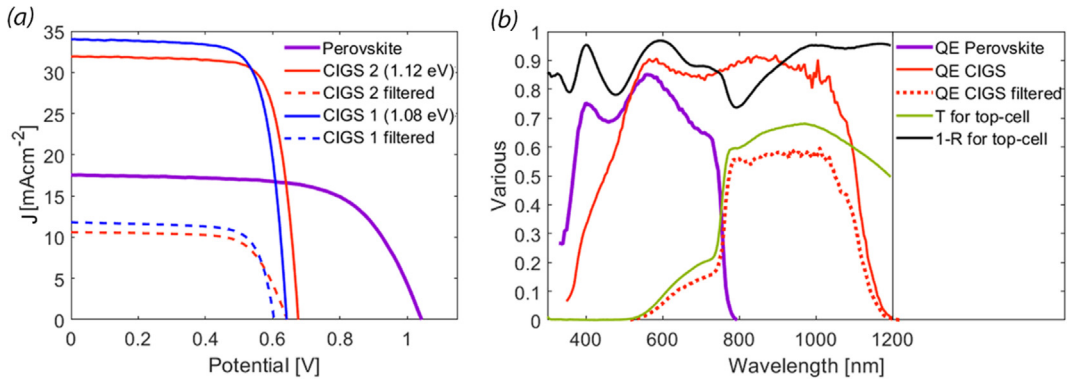

Fig. 5. (a) JV-curves for a standalone semi-transparent perovskite top cell and for two CIGS cells based on smooth CIGS with two different band gaps (1.08 and 1.12 eV). The JV-characteristics for the CIGS cell were measured both under standard illumination and while filtered by the perovskite top cell. (b) QE-data for the perovskite top-cell and CIGS bottom-cell (filtered by the top cell and under standard illumination) compared to transmission and reflectance of the perovskite top-cell.

sample area of 0.05 cm^2. The devices performance for the devices varied from zero to 16% depending on synthesis details (Fig. 6b). For the first part of the project, the performance was generally low, and the sample variation was large, both with respect to sample-to sample, batch-to batch, and sub cell-to sub cell variations. In those cases, only data for the best cell on each substrate is reported. Later in the project, both sample homogeneity and device performance increased, whereupon we switched to report average cell performances (see SI for details). Details concerning stack sequences, depositions parameters, and IV-response for all cells are provided as a supplementary CVS-file. It is worth to point out is that the best 2-terminal tandem cells are close in performance to the 4-terminal setup described above. This illustrates that for the best cell configurations, the interface physics of the two sub cells works well (Fig. 6b). What follows is an account of what we learned and observed during the project in the form of a layer-by-layer discussion of the device stack.

3.4.1. CIGS and the CdS-buffer layer

The initial uniformity in performance over the sample surface for both the CIGS and the semi-transparent perovskite cells was good, when measured as single junction devices. The same could not be said for the resulting tandem cells. From tandem cells based on shunted CIGS-bottom cells we could, however, still observe high fill factors, i.e. up to 70%, indicating that the perovskite top-cells, at least locally, could function well also when deposited on top of the CIGS-stack.

One potential cause of the problem with both performance and homogeneity is the surface roughness of the CIGS stack. For the CIGS-layers initially used showing high roughness (Fig. 4h), we could produce good CIGS cells and a few good tandem cells, but not tandem cells with good homogeneity over the sample surface. Because of this, the CIGS deposition process was switched to one that in general produces smoother CIGS. In addition, the CIGS in this process was further modified by alloying it with Ag into (Ag, Cu)(In, Ga)Se_2 (ACIGS), which result in an even smoother film as the Ag inclusion promotes grain growth. The resulting smooth ACIGS turned out to be a key to improve the tandem performance, especially in terms of homogeneity, which is in line with previous reports pointing out the CIGS roughness as a problem.

Cross section SEM-images of tandem cells based on a smoother version of CIGS reveal large grains and a mostly flat surface (Fig. 7a). Even if those CIGS surfaces are considerably flatter than the ones from our other process (Fig. 4f and h), there are deep crevices between some of the grains. The top surface of the tandem stack is, however, rather flat. That means that the perovskite spin-coating level out some of the surface roughness, with the consequence that the perovskite thickness can vary quite dramatically over the sample surface. From a device perspective, a partially thicker perovskite layer is considerably more benign than one that is partially thinner and penetrated by layers underneath. Not only roughness per se but also the roughness topology thus plays an important role.

The CIGS deposition is, however, not the only cause of inhomogeneities and surface roughness. In a few batches we observed an inhomogeneity with patterns stretching over multiple substrates, thus originating from process steps before cutting up the substrates. The probable cause was the chemical bath deposition (CBD) of the CdS buffer layer, which is known to be an additional source of surface roughness. In our standard CdS process, we use thiourea, cadmium acetate, and ammonia. Ammonia is consumed in the process when CdS is formed which result in a change of both pH and growth rate during the process. With time, the pH decreases, which increases the growth rate and eventually also leads to CdS nucleation in the solution. When the process is finished, a sufficiently thick CdS film has formed on the sample, but there are also CdS particles in the solution that can be a few hundred nm in diameter, and some of those may be incorporated in the

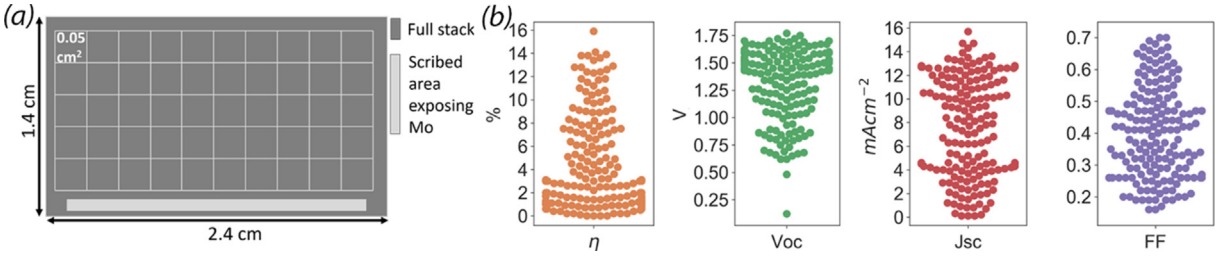

Fig. 6. (a) Geometrical layout of samples with substrates measuring 2.4 · 1.4 cm on which 50 individual cells with an individual sample size of 0.05 cm^2 were defined by scribing. (b) Spread in device performance for the full sample set of 2-terminal CIGS-perovskite devices. The early samples had large cell-to-cell variations and for those, the best cell on each substrate is reported. For later cells that generally had better performance as well as lower sample-to-sample variations, it is the average performance that is reported. See SI for further details.

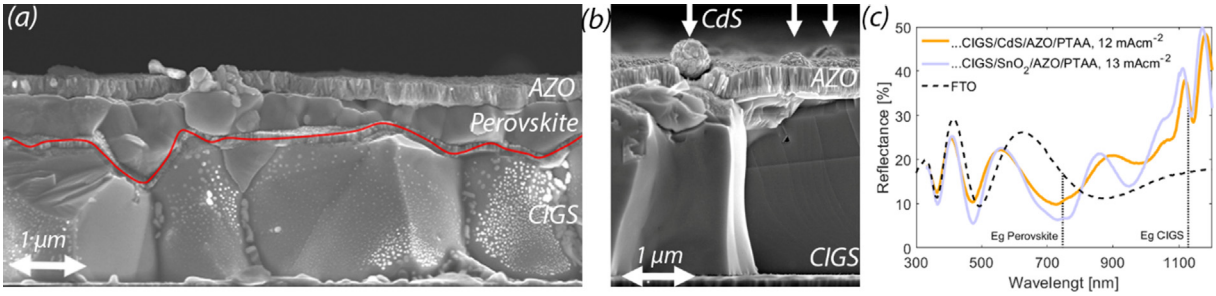

Fig. 7. (a) A cross section SEM image of a CIGS-perovskite tandem cell based on reasonable flat CIGS. The device stack for the specific image is SLG/Mo/ACIGS/CdS/i-ZnO/ZnO:Al/NiO/PTAA/perovskite/PCBM/SnO_2/ITO. A read line is highlighting the surface profile of the CIGS. (b) Cross section SEM of a CIGS/CdS/AZO film showing how a CdS particle generate an additional protrusion. (c) Reflection for two tandem stacks using either CdS deposited by CBD or SnO_2 deposited by ALD.

growing CdS film at a rather late stage. In SEM images, it can look like such particles are sprinkled over the CIGS surface, and Fig. 7b shows a cross section of a CIGS/CdS/AZO film showing the kind of protrusions this can create. These particles are benign from a CIGS-cell perspective, but they are potentially problematic for creating covering shunt-free films with subsequent spin-coating procedures.

One way to decrease CdS particle formation is to decrease the chemical bath deposition time, and consequently also the film thickness. The trade-off is that a thinner CdS film may increase CIGS surface recombination losses. We dedicated one sample series towards exploring the effect of a thinner CdS layer (SI). We observed that reduction of the CdS thickness resulted in a slight decrease in all solar cell parameters, i.e. Voc, Jsc, FF, and η, for the resulting tandem cells, with a larger drop for the thinnest films (SI).

To explore another alternative, we made one cell configuration where the CdS was replaced with SnO_2 deposited by ALD, where the ALD process ensures a smooth covering film without introducing any additional particles or surface roughness. The switch to SnO_2 resulted in both higher current and cell efficiency, despite the fact that SnO_2 in normal CIGS-cell is a less well performing buffer layer (Hultqvist et al., 2012). This could potentially be a double effect. ALD deposition leads to smoother films, and we also observed a slight decrease in reflectance of the tandem stack (Fig. 7c).

The best tandem cells produced in this project were obtained with the smoother CIGS and standard deposition of CdS. The data does, however, indicate that either optimising the CdS deposition with respect to particle formation, or going for a vacuum deposition process for the buffer layer will be a viable strategy for further increasing the tandem performance.

3.4.2. The mid TCO

On top of the CdS-buffer layer, a transparent conductive oxide (TCO) is deposited. For CIGS, the standard TCO is composed of 75 nm thick intrinsic ZnO (i-ZnO) followed by a 200 nm thick aluminium doped ZnO (Al:ZnO or AZO) layer. This composition has been our baseline in the tandem devices.

The requirements in terms of conduction, transparency, and energy alignment for this TCO layer are different in tandem cells compared to standard CIGS. In a tandem stack, where the top-cell absorbs the high-energy photons, a low absorption in the mid TCO is no longer required for that energy region. Decreasing the parasitic absorption in the NIR/IR-region is on the other hand more important as that is the only light reaching the bottom-cell. This could potentially be accomplished by decreasing the layer thickness, which is a viable approach as the tandem cell only requires vertical conduction through the mid TCO, in contrast to the lateral conduction required for current collection in standalone CIGS-cells.

This was explored by varying the AZO thickness, i.e. 6, 12, 25, 50, 100, and 200 nm (Fig. 8a). Data scatters a bit, and the variation is larger than what could be explained by differences in parasitic absorption. What we can conclude is that it is possible to thin down the AZO quite a lot, i.e. down to 12 nm, and still obtain functional tandem devices. Although data is inconclusive, there appears to be a trend towards higher top performance, but also a larger spread with more failed cells, when the AZO becomes thinner (Fig. 8a and SI).

An alternative to AZO is ITO (In-SnO_2), which has the benefit of higher mobility and thus a lower carrier density for the same conductivity and thereby lower NIR-absorption. Based on the data, we cannot conclude that there should be a significant difference between using ITO or AZO (Fig. 8b). It does, however, appear as if the ITO can be made thinner than the AZO without compromising the cell performance. 7 nm ITO were used in functional devices whereas 6 nm AZO appears to be too thin.

In standard CIGS, the i-ZnO is not strictly necessary, but reduces the risk for failed cells. We performed tests to see if the i-ZnO could be removed from the tandem stack. Our tests indicate that the i-ZnO not is strictly necessary as long as there is a thin layer of either AZO or ITO, but the data does not give support for removing the i-ZnO from the baseline-procedure (see SI). The TCO does, however, appears to be necessary and the two tandem samples that were produced without either ITO or AZO had both failed cells. Depositing the NiO hole-conductor directly on the CdS also resulted in failed devices.

3.4.3. The HTL

To connect the CIGS and the perovskite, a contact layer acting as a substrate for the perovskite should be deposited on the mid-TCO. This layer must have the right energy alignment and function as a hole-selective contact (or hole transport layer, HTL) with respect to the perovskite, and its deposition should not harm the CIGS-stack. Several HTL materials have been demonstrated that potentially could be used in in this architectures, e.g. NiO (Lai et al., 2015; Seo et al., 2016), CuI (Sun et al., 2016), CuO (Rao et al., 2016), CuSCN (Ye et al., 2015; Qin et al., 2014), AlO_x (Wei et al., 2015); PTAA (Saliba et al., 2018a), etc.

Several groups have demonstrated reasonably good p-i-n perovskite cells with NiO HTL (Hu et al., 2017; Xie et al., 2017; Wu et al., 2017; Chen et al., 2016, 2017; Bai et al., 2017; Xue et al., 2017), deposited with a range of methods including: spin-coating (He et al., 2018; Hu et al., 2017; Chen et al., 2017; Bai et al., 2017; Nie et al., 2018; Wei et al., 2018), spray-coating (Xie et al., 2017; Wu et al., 2017; Xiao et al., 2019), electrodeposition (Park et al., 2017), e-beam evaporation (Pae et al., 2017), sputtering (Li et al., 2017; Islam et al., 2017; Cui et al., 2014), pulsed laser deposition (Park et al., 2015), and ALD (Jost et al., 2019; Seo et al., 2016). This shows that NiO has a reasonable broad parameter window of HTL functionality. NiO also has the benefit of good stability, earth abundance, and compatibility with vacuum deposition procedures. Our initial NiO experiments also showed more promise than other alternatives. Therefore, we primarily used sputtered NiO as the HTL in this work.

Unfortunately, the NiO chemistry is rich and complicated with a variable Ni:O stoichiometry (Islam et al., 2017), different phases (Ciro et al., 2017), and a number of possible surface oxides, hydroxides, and oxyhydroxides (Li and Selloni, 2014; Van der Ven et al., 2006); all of

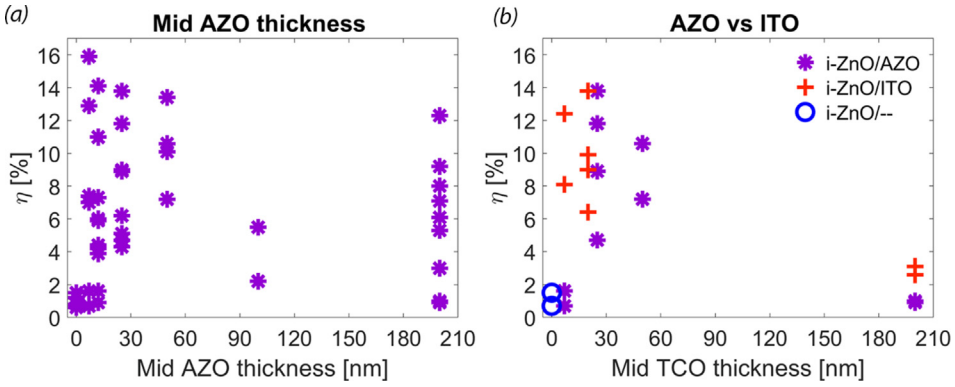

Fig. 8. (a) Impact on the thickens of the mid ZnO:Al layer. For devices with the device stack, SLG/Mo/CIGS/CdS/*i-ZnO/Al:ZnO*/NiO/Perovskite/LiF/PCBM/TCO. (b) Difference between ITO and ZnO:Al as the mid TCO as a function of thickness. For devices with the device stack, SLG/Mo/CIGS/CdS/*i-ZnO/Al:ZnO or ITO*/NiO/Perovskite/LiF/PCBM/TCO.

which could influence the interaction with the perovskite and the functionality in the device stack. We will discuss the complexity of NiO as an HTL in detail in a parallel paper.

Our device stacks with sputtered NiO on top were stored in air and without further treatment introduced in a nitrogen-filled glove box just before perovskite deposition. Based on work on p-i-n cells on FTO/NiO substrates, we can note a few points: UV-ozone treatment changes the Ni:O stoichiometry in a way that is detrimental for device performance; spin-coated and sputtered NiO give similar device performance; and adding a monolayer of surface dipoles appears to be beneficial but is non-trivial to reproduce in a consistent manner. The untreated NiO works as a decent baseline, but with additional work on the NiO/perovskite interface, we expect to improve the device performance further.

The NiO thickness was varied between 7 and 45 nm in the tandem stack. A weak trend towards higher Jsc and η was observed with decreasing films thickness, even if the spread in performance was larger for the thinnest films (SI). The trade-off appears to be higher absorption for thicker films and increased risks for shunts due to incomplete coverage for thinner films. 15–20 nm seems to be a reasonable compromise.

Besides NiO, we also performed experiments with PTAA (poly triaryl amine), which is one of the most commonly used HTL in perovskite devices with the p-i-n architecture. Spin-coated PTAA was used as the sole HTL in two tandem samples. Both samples had cells where the top-cell appeared to be shunted, and thus failed to show a tandem voltage and instead behaved similar to a shaded CIGS-cells. That is in contrast to the control cells on SLG/FTO substrates where PTAA and NiO resulted in cells with similar performance. The PTAA failure is possibly a surface roughness effect. Efficient PTAA based p-i-n devices are often deposited on flat ITO substrates. Spin-coating thin films on rough substrates is difficult, as film coverage easily gets incomplete over hills and protrusions of the substrates that could penetrate the film. Even the smoother CIGS-stacks here used could with their cracks and crevices (Fig. 4g and i) have been too rough for the PTAA to be fully covering. Sputtering, as done with NiO, may thus simply give better HTL surface coverage.

Jost et al. (2019) have published a paper that suggested that a double HTL composed of NiO covered with PTAA would be beneficial in CIGS perovskite tandem cells. By comparing pairs of cells produced in this study where the use of NiO or NiO/PTAA is the only difference, NiO/PTAA appears beneficial, in particular regarding homogeneity (Fig. 9a). Curiously, the layer underneath the NiO seems to influence to which extend a PTAA layer is beneficial (Fig. 9a). The data is limited but in the device stack CdS/i-ZnO/Al:ZnO/NiO/PTAA, the PTAA layers appears to have a beneficial effect. If the i-ZnO is omitted, the effect does, however, disappear, and if the i-ZnO/Al:ZnO is replaced with 15 nm sputtered ITO, the devices without PTAA performs better. The standalone p-i-n perovskite cells with FTO/NiO also performed slightly better without PTAA.

The greatest benefit we found with PTAA, at least in conjunction with i-ZnO/Al:ZnO/NiO substrates, is homogeneity over the sample surface. With PTAA in that configuration, the variation between samples on the same substrates decreased (Fig. 9d–g). Based on that observation, we shifted our baseline procedure towards using a double layer of NiO/PTAA as HTL.

The interplay between the mid-TCO, the NiO, the PTAA, and the perovskite is still unclear. We speculate that there could be a surface roughness complementarity between NiO and PTAA. Spin-coating a thin PTAA layer on a rough surface will lead to incomplete surface covering, resulting in shunts, especially where the layer below has regions that vertically protrude from the surrounding. NiO sputtering gives better surface coverage, but has problems with covering deep valleys in the substrates, which are the parts that spin-coating is good at filling. Another hypothesis is that NiO acts as the primary HTL whereas the PTAA's primary benefit is to provide a better interface towards the perovskite, which both is hole selective and has the right energy alignment. That is a hypothesis strengthened by the observed benefit an extra surface dipole on the NiO surface can have, but it is weekend by the fact that our champion device, with a small margin, was made without PTAA.

The beneficial effect of an additional PTAA layer is, however, probably limited in importance, unless the cell is bad from the start, and when looking at the complete sample set (Fig. 9b) the difference essentially disappears, even if there is a considerably smaller spread in Voc while incorporating PTAA (Fig. 9c). The similarity in performance for the cells on NiO and NiO/PTAA indicate that even if not perfect, this interface towards the perovskite may not be our primary performance bottleneck.

3.4.4. *A note on the perovskite layer*

Our baseline perovskites have the composition Rb-$Cs_{0.05}FA_{0.79}MA_{0.16}PbBr_{0.49}I_{2.51}$ and $Cs_{0.05}FA_{0.79}MA_{0.16}PbBr_{0.49}I_{2.51}$, but we also tested other compositions. One of those was $Cs_{0.17}FA_{0.83}PbBr_{0.51}I_{2.49}$, which is interesting from a stability perspective as it excludes the MA ions which appear to be a trigger for decomposition (Zhou and Zhao, 2019).

In our early experiments, the MA-free perovskites performed better than the baseline composition (Fig. 10a) which we also observed in p-i-n cells on FTO/NiO. That is interesting as it contrasts the behaviour of the standard n-i-p-control cells, which in this experimental round had an average efficiency of 15.7% (five cells) compared to 10.8% (five cells) for the MA-free counterparts. As the tandem efficiencies for those cells were rather low (Fig. 10a), the perovskite was likely not the limiting factor and we therefore continued to use the baseline compositions for proof of concept based on their short-term higher potential for maximum efficiency. The MA-free perovskites are due to their increased stability interesting candidates for final applications, making their initial favourable performance an interesting observation.

Towards the end of the project when the electronics of the cells work reasonably well, we aimed at improving the optical matching by

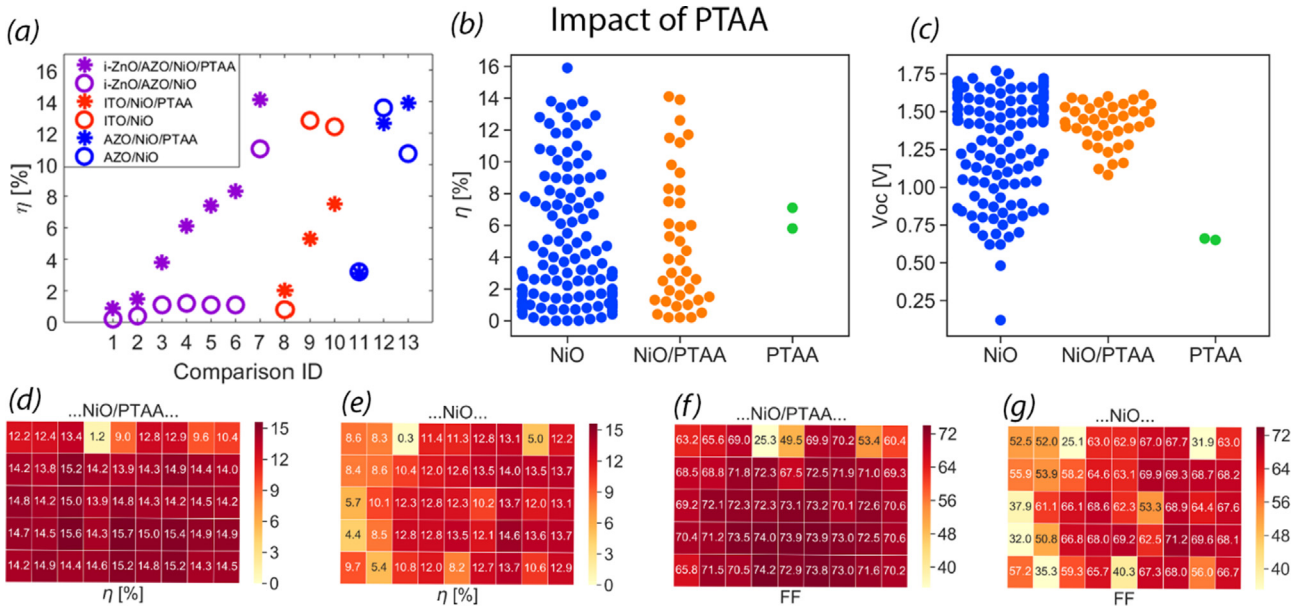

Fig. 9. (a) Comparing performance of pair of cells where the only difference is the HTL where either NiO or NiO/PTAA were used. (b) Spread in performance for the entire sample set with respect to the HTL used. (c) The spread in Voc for the full sample set with respect to the HTL used. (d, e) Illustration of sample homogeneity of η and FF for cells with (d, f) and without (e, g) PTAA. Sample ID 130 and 131. For Voc and Jsc, se SI.

increasing the perovskite band gap. This was done by varying the bromide content in three steps: 23%, 38%, and 45%, resulting in band gaps of 1.66 eV, 1.77 eV, and 1.83 eV (SI). An increased bromide content increases the band gap Eq. (2), but there is a balance as too much bromide could trigger reversible light induced phase separations at the expense of device performance. A slight increase in Voc was observed in the control cells for the composition with 38% Br, but both Voc and FF dropped with a bromide content increased to 45% (Table 2), indicating that this pushed it too far. The increased band gap did not lead to a general increase in the tandem efficiencies (Fig. 10b and Table 2) even if two cells performed reasonably well with the highest band gap perovskite. Given the higher transparency and the expected higher current density in the bottom cells (Fig. 1), more could have been expected indicate that other bottlenecks are present as well which will be elaborated below.

3.4.5. The ETL layer

For a working tandem cell, the perovskite must be covered by an electron selective contact (ETL), which must have the right energy alignment, be electron selective with respect to charge carrier injection from the perovskite, and be transparent from IR to UV. The ETL deposition should not harm the perovskite, which restricts the annealing temperatures and excludes most common solvents. A large number of potential ETLs have been described in the literature, out of which we tried several in this work (Fig. 11a, Table 3, SI).

A-priori, SnO_2 appears to be an ideal ETL. SnO_2 is stable, transparent, can be deposited by atomic layer deposition (ALD) at low temperatures, is a good substrate for subsequent TCO sputtering, and not as photocatalytic as the TiO_2 commonly used in n-i-p architectures. We also have previous experience with ALD deposition of SnO_2 on FTO for high-efficiency n-i-p perovskite cells (Baena et al., 2015). Despite this, we did not manage to deposit SnO_2 directly on top of perovskites in a way leading to good cell performance (Fig. 11a). To our knowledge, neither have other groups. XRD, XPS, and UV–vis analysis show that we can deposit SnO_2 on top of perovskites without detecting any changes in the SnO_2 or the perovskite, but we have preliminary results suggesting that the ALD process leads to a change in the perovskite/SnO_2 interface with detrimental results for device performance. We have explored this in some detail, and will return with a full report in another paper.

The most frequently used ETL for p-i-n perovskite cells is probably PCBM. The PCBM is commonly spin-coated from a chlorobenzene solution, and given the spread of concentrations, spin-coating parameters, and annealing procedures reported (Bai et al., 2017; Seo et al., 2016, 2014a; Chang et al., 2017; Zhou et al., 2018; Chen et al., 2015), the parameter window of applicability appears to be reasonably broad. In our cells, thicker spin-coated PCBM films, i.e. films spun from more concentrated solutions, decreased the cell performance, indicating transport problems, whereas thinner films more frequently resulted in failed devices, potentially due to incomplete surface coverage (SI). We struggled in finding the right balance, and out of 170 FTO/NiO/

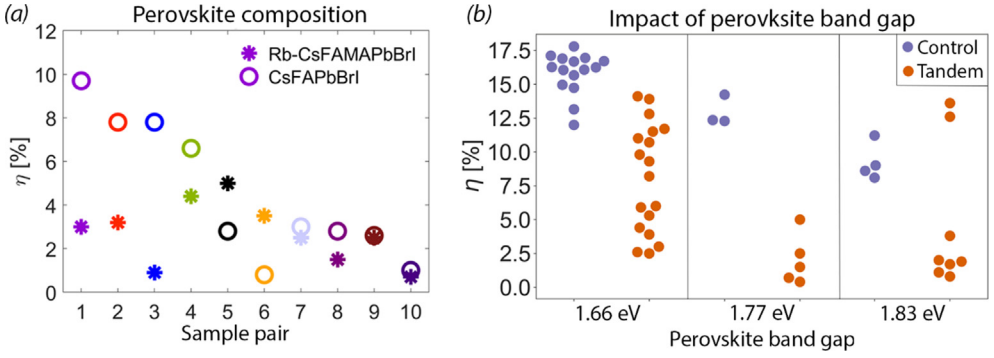

Fig. 10. (a) Comparing tandem cells with MA and without MA for devices with the following stack CIGS/CdS/i-ZnO/ZnO:Al/NiO/Perovskite/C60/SnO_2 (various thicknesses)/(i-ZnO or not)/ZnO:Al. For each pair of cells in the comparison, only the perovskite composition differs. Data is sorted in order of decreasing efficiency. (b) Efficiency of both control cells (FTO/TiO_2/Perovskite/Spiro/Au) and the corresponding tandem cells as a function of perovskite band gap.

Table 2
Cell performance for both n-i-p control cells and tandem cells for three different perovskite band gaps. Tandem cells had the deice stack CIGS/CdS/TCO(*various*)/NiO/Perovskite(*various*)/LiF/PCBM/SnO_2/ITO. The control cells had the device stack FTO/TiO/mp-TiO/Perovskite(*various*)/Spiro/Au. NoC refer to the number of cells with that configuration and ID refers to the position in the data table given in the SI. Eg is given in eV, Voc in V, Jsc in mA/cm^2, PCE in %, and FF is a unitless quantity.

					Best Cell				Average Cell			
Perovskite	Eg	Architecture	NoC	ID	Voc	Jsc	FF	PCE	Voc	Jsc	FF	PCE
$Rb\text{-}Cs_{0.05}FA_{0.77}MA_{0.23}PbBr_{0.68}I_{2.32}$	1.66	Controll	15		1.14	21.4	0.73	17.8	1.11	19.6	0.73	15.8
$Rb\text{-}Cs_{0.05}FA_{0.75}MA_{0.25}PbBr_{1.10}I_{1.90}$	1.77	Controll	3		1.16	16.6	0.74	14.2	1.14	16.3	0.69	13.0
$Rb\text{-}Cs_{0.05}FA_{0.67}MA_{0.33}PbBr_{1.31}I_{1.69}$	1.83	Controll	4		1.13	15.7	0.64	11.2	1.09	13.5	0.63	9.2
$Rb\text{-}Cs_{0.05}FA_{0.77}MA_{0.23}PbBr_{0.68}I_{2.32}$	1.66	Tandem	18	130	1.58	13.0	0.70	14.1	1.43	9.9	0.54	8.1
$Rb\text{-}Cs_{0.05}FA_{0.75}MA_{0.25}PbBr_{1.10}I_{1.90}$	1.77	Tandem	5	149	1.50	6.3	0.50	5.0	1.30	4.0	0.35	2.0
$Rb\text{-}Cs_{0.05}FA_{0.67}MA_{0.33}PbBr_{1.31}I_{1.69}$	1.83	Tandem	8	139	1.59	12.6	0.67	13.6	1.42	5.6	0.46	4.7

perovskite cells with spin-coated PCBM, the average efficiency was below 5% and the top results around 12%.

The tandem cells with spin-coated PCBM only reached a few percent efficiency (Fig. 11a). Cross section SEM-images show that the perovskite deposition evens out roughness of the previous layers, but given initial problems with rough CIGS, this could not be excluded as a cause of failure. Surface roughness related problems of previous layers could also overshadow differences between our different ETL depositions, introducing an additional uncertainty in how to interpret the data.

Another commonly used ETL is C60 (Saliba et al., 2018a), which electronically behaves essentially the same as PCBM. Without a functionalised side chain enabling solubility in perovskite compatible solvents, C60 is difficult to spin coat and was instead evaporated. That is, however, not necessarily a drawback, as evaporation could give better surface coverage for thin layers on rough surfaces. In our tandem cells, C60 led to higher efficiencies for the tandem devices than spin-coated PCBM (Fig. 11a). That is in contrast to the control cells where they resulted in similar performance.

At this stage, SnO_2 directly on top of the perovskite did not work at all and spin-coated PCBM and evaporated C60 worked but not particularly well. We then decided to try a multi stack approach. The rational is that a thin buffer layer on top of the perovskite possibly could protect the perovskite surface during subsequent SnO_2 deposition. PCBM and C60 are natural candidates for such a buffer layer as they can act as an ETL in their own right. Together with SnO_2, their functionality reduces from a primary ETL towards an energetically aligned and chemically inert surface protection layer during SnO_2 nucleation

Depositing SnO_2 on top of spin-coated PCBM led to good efficiencies in the control cells, but besides one outlier, it did not improve the tandem performance (Fig. 11a). C60 worked better as a buffer layer, and our best tandem cell efficiency increased to 10% (Fig. 11a and Table 3). This demonstrate that SnO_2 can be used as an ETL layer as long as a buffer layer is used to protect the perovskite surface during ALD deposition. In one cell, the PCBM was evaporated instead of spin-coated, and in that cell the tandem efficiency increased to 12.8% (Fig. 11a). The CIGS used for that cell was smoother than the ones used before, which obscures a direct comparison and the control cells did not show a clear difference between using evaporated PCBM or C60, but it nevertheless convinced us to switch to evaporated PCBM buffer layers for the subsequent cells.

A so far not fully supported hypothesis is that evaporation speed is more important for PCBM than for C60, and that a lower evaporation speed of PCBM is significantly better than a faster one. At a lower evaporation rate, i.e. lower temperature, the PCBM left in the tungsten boat after evaporation has a compact, black, and shiny appearance, whereas at a higher evaporation rate, i.e. higher temperature, it obtains a fluffier, mat, sponge-like texture.

Concerning the thickness of the evaporated PCBM/C60, 10 nm or slightly thinner appears to be a reasonable compromise between surface protection and transport limitations. For the SnO_2 layer, the trade-off appears to be that thinner is better, but that thinner also increase risk of failure. The clearest trend we observed in terms of thickness is a decrease in the fill factor with increased thickness (Fig. 11b). As a reasonable compromise, we used 75 ALD cycles, which correspond to a thickness of approximately 4–7 nm (depending on nucleation dynamics).

In a paper by Bush et al. (2017) focusing on silicon-perovskite tandems, the stack sequence LiF/PCBM/SnO_2 was proposed as a good ETL. LiF is a high band gap insulator that can be used as an antireflective coating (Bush et al., 2017; Ateto et al., 2016), and a thick LiF layer would effectively block current transport. A few nm thin layer could, however, possibly passivate shunts (Bush et al., 2017), improve the interface characteristics without impairing the current flow (Seo et al., 2014b), and reduce surface recombination (Stolterfoht et al., 2018). LiF was also claimed to improve the consistency in the device performance (Bush et al., 2017).

Although the variations in the efficiency is rather large in the multilayer devices, our best tandem cells incorporated a 1 nm LiF layer (Fig. 11a). The LiF also improved the top performance for all ETL configurations tested in the control cells deposited on FTO/NiO. The surface covering of this thin layer is most likely incomplete.

3.4.6. The top TCO

The device stack is finalised by a TCO layer. The standard TCO for CIGS is 80 nm of i-ZnO, which not is particularly conductive, followed by 300 nm of ZnO:Al. That was also used as the baseline for the tandem

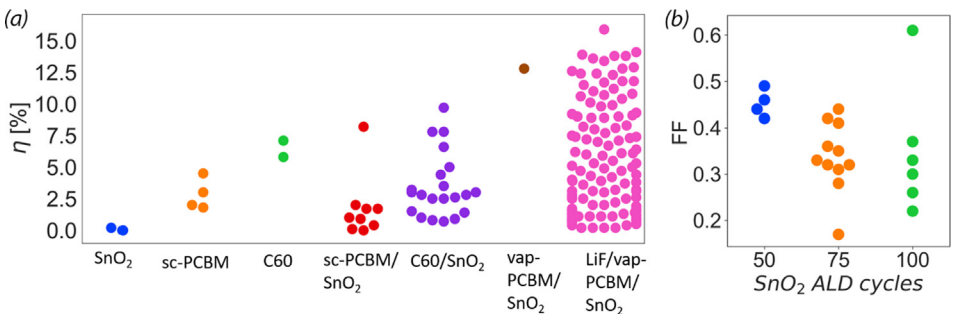

Fig. 11. (a) Efficiency for tandem devices for the different ETL explored. Corresponding figures for Voc, Jsc, and η are found in the SI. sp for spin coated, vap for evaporated, (b) Trend in FF with respect to number of ALD cycles used for SnO_2 deposition for cells with the ETL sequence C60/SnO_2. Corresponding figures for Voc, Jsc, and η are found in the SI.

Table 3
The effect of different electron transport layers on the device performance. Voc in given in V, Jsc in mA/cm^2, PCE in %, and FF is a unitless quantity. Spin-c for spin coated. Vap for evaporated.

ETL	NoC	Best cell					Average cell			
		ID	Voc	Jsc	FF	PCE	Voc	Jsc	FF	PCE
SnO_2 (~10 nm, ALD)	2	3	0.80	0.7	0.41	0.2	0.75	0.4	0.36	0.1
PCBM60 (spin-c)	4	34	1.52	12.0	0.26	4.5	1.48	8.4	0.22	2.8
PCBM60 (spin-c) | SnO_2 (~10 nm, ALD)	9	38	1.50	10.5	0.54	8.2	1.20	3.7	0.33	1.8
PCBM60 (vap) | SnO_2 (~10 nm, ALD)	1	51	1.65	11.6	0.67	12.8	1.65	11.6	0.67	12.8
C60 (25 nm, vap)	2	36	0.66	15.7	0.70	7.1	0.66	14.2	0.70	6.5
C60 (25 nm, vap) | SnO_2 (~10 nm, ALD)	21	15	1.63	14.7	0.61	9.7	1.04	8.8	0.36	3.5
LiF (1 nm, vap) | PCBM60 (10 nm, vap) | SnO_2 (~10 nm, ALD)	123	66	1.77	14.7	0.70	15.9	1.40	7.9	0.42	5.5

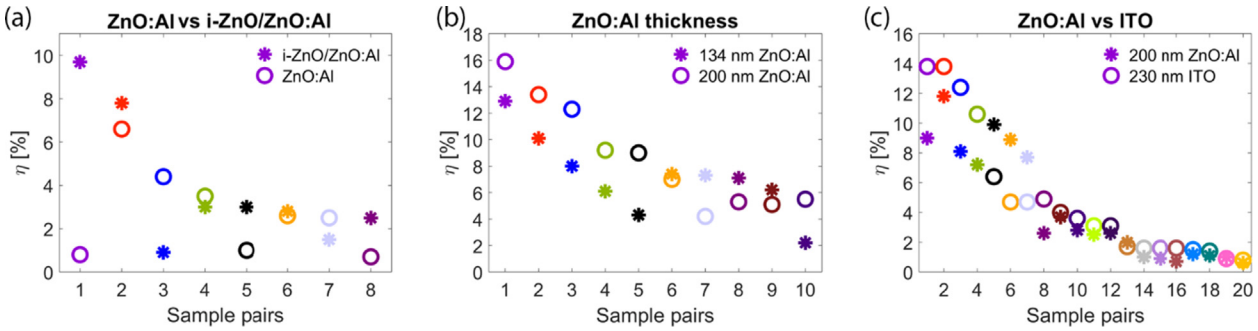

Fig. 12. Comparing performance of pairs of cells with: (a) i-ZnO or not. (b) Different ZnO:Al thicknesses, and: (c) The use of either ZnO:Al or ITO as the top TCO. In all figures, sample pairs are compared where the only difference is the parameter under exploration. Samples are sorted in order of descending top efficiency. The device stack for cells in (a) was CIGS/CdS/i-ZnO/NiO/Perovskite/C60/SnO_2/(*i-ZnO or not*)/ZnO:Al and in (b) and (c) CIGS/CdS/i-ZnO/NiO/Perovskite/LiF/PCBM/SnO_2/*ZnO:Al or ITO*.

cells. In our control cells, a TCO deposited directly on PCBM or C60 resulted in mediocre cell performance. If that is due to a non-optimal energy band alignment or interface chemistry is still unclear, but incorporation of a SnO_2 layer resulted in substantially better performance.

To explore the role of i-ZnO in CIGS-perovskite solar cells, devices with, and without i-ZnO in the top TCO was made. In 8 sample pairs (Fig. 12a), we observed no clear trends, and to reduce the stack complexity, the i-ZnO in the top TCO was excluded in subsequent cells.

The front contact is a source of parasitic absorption, especially in the IR-region. We therefor made an attempt to decrease the ZnO:Al thickness. A thicker ZnO:Al generally resulted in better cells performance, especially for the better cells (Fig. 12b). The largest difference was in the FF (SI), indicating that TCO resistance was more of a bottleneck than absorption, at least for those devices.

An alternative to ZnO:Al is ITO, which has similar conductivity but lower IR-absorption due to lower free charge carrier density (SI). The data is inconclusive, but cells with ITO were on average better than cells with ZnO:Al (Fig. 12c), and from the JV-data cells with ITO appears to have a somewhat higher ideality factor and a bit lower series resistance.

In a full-scale cell, a metal grid would be evaporated on top of the TCO. That is standard procedure for lab cells, but not for interconnected monolithic modules. With a cell area of 0.05 cm^2, that is not necessary and we contacted the measurement probes directly on top of the TCO.

3.5. A note on optical matching

In our initial exploration, we used standard compositions for both the perovskites and the CIGS. Those were not perfectly band gap matched, which is something that must change in order to reach higher efficiencies (Fig. 13a). The precise band gap values required for a match of the CIGS and the perovskite depend on the thickness of the perovskite and the optical characteristics of every layer in the stack, and will require a detailed optical analysis to optimise. The optimisation will most probably result in a higher perovskite band gap and a lower CIGS band gap than used here.

In the tandem cells based on perovskites using our standard composition, the photocurrent was lower than what would be obtained from the top cell alone (Fig. 5). By increasing the band gap of the perovskite, thus increasing the light flux to the bottom cell, an increase in the tandem photocurrent is expected, given that current generation on the bottom cell is limiting. With the exemption of two tandem samples, we observed the opposite response (Fig. 13b). In part, this is due to the perovskite performance decreasing when the bromide content increases beyond our standard composition (Table 2). The decrease in perovskite performance could, however, not explain the entire decrease in tandem performance, which given transmission and current density is expected to be higher. This indicate that there may be a band alignment problem that increases when the perovskite band gap increases, and that there thus are more than the transparency of the top cell which is limiting the photocurrent of the tandem cell.

Efforts were also made to decrease the band gap of the CIGS. Unfortunately, the performance of our CIGS cells deceased with decreasing band gap in this series (Fig. 4b), offsetting the expected benefit of a lower band gap. By comparing specific cells where the CIGS performance was similar, despite different band gaps, the expected increase in performance was indeed observed. This is illustrated in Fig. 13c and Table 4, where the performance of the tandem cells increased close to 2% units when the CIGS band gap decreased from 1.09 to 1.01 eV (Fig. 13c).

3.6. Concerning the cross section of the device

Three elemental maps showing the interfaces in different magnifications and their corresponding bright field STEM images are depicted in Fig. 14f. Fig. 14a and d shows that the layer thicknesses of the CdS (60 nm), the ZnO (90 nm), and the NiO (20 nm) are homogeneous. A

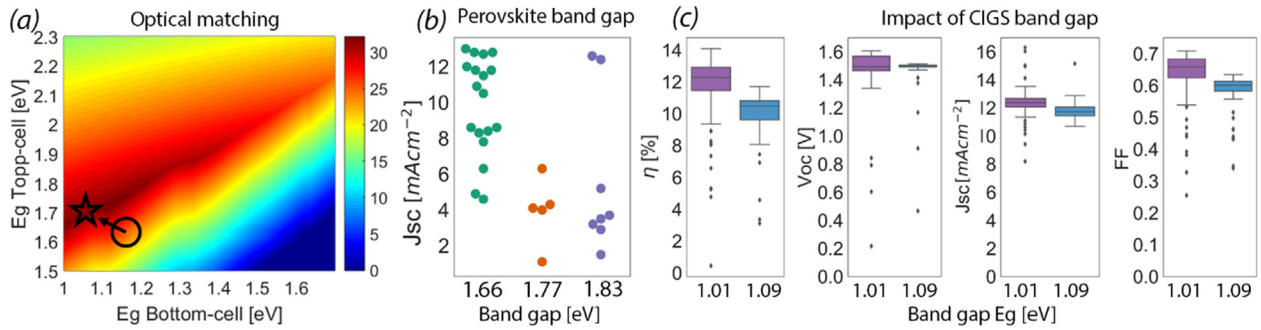

Fig. 13. (a) An illustration of the deviation from band gap matching between the CIGS and the perovskites used for much of the explorations done in this project. The black circle represents where we are, and the black star the ideal point. (b) Jsc as a function of perovskite band gap for tandem samples with the device stack CIGS/CdS/TCO (*various*)/NiO/Perovskite (*various*)/LiF/PCBM/SnO_2/ITO. (c) Impact of the CIGS band gap for cells based on CIGS with similar performance. The device stack for those cells were CIGS/CdS/ZnO:Al/NiO/Perovskite/LiF/PCBM/SnO_2/ITO.

Table 4
Performance of tandem cells based on similar performing CIGS with different band gaps. The bottom cell is the same for every tandem cell with a specific ID. The tandem cell data is given as an average over 45 cells on each sample with a unique ID. Eg is given in eV, Voc in V, Jsc in mA/cm^2, PCE in %, and FF is a unitless quantity.

		Bottom Cell				Tandem cell			
ID	Eg CIGS	Voc	Jsc	FF	PCE	Voc	Jsc	FF	PCE
141	1.09	0.544	32.9	0.71	12.8	1.45	11.8	0.57	9.8
146	1.01	0.513	34.5	0.71	12.6	1.50	12.7	0.61	11.7
148	1.01	0.509	34.4	0.71	11.7	1.45	12.0	0.65	11.5

distinction between i-ZnO and ZnO:Al is not possible.

The issue about the CdS particles attaching to the CdS layer from the CdS solution-based deposition process is apparent in Fig. 14b and e, where such a particle is observed. This particle measures a diameter of ca. 150 nm, although absolute thickness cannot completely be determined and should be assumed larger, since it is a cross-section and the particle has probably not been cut through the center. The CdS particle is covered, but not fully encapsulated with ZnO and NiO by the subsequent deposition processes. A closed film of PTAA is not detected by STEM-EDX, but accumulations of carbon are observed in the valleys of the NiO film and around the bottom of the CdS particle. A third map (Fig. 14c and f) with higher magnification was recorded to find such possible thin layers of PTAA, but no such film with enhanced carbon content is observed. Although unlikely since not detected, the presence of a thin (< 2 nm) PTAA film cannot completely be ruled out due to experimental constraints, such as lateral resolution and sample thickness. This lack of observing the PTAA layer is in line with reasoning above of the complementarity between NiO and PTAA where it was assumed that spin-coated PTAA not form a covering film but accumulates in crevasses in the film.

The perovskite layer, displayed by the Pb signature, is not uniformly thick and varies between 240 nm and 470 nm in the thinnest and thickest region respectively (Fig. 14a and d). The PCBM (13 nm), as recognized by the carbon film, and SnO_2 (5 nm) layers are evenly thick. The STEM bright field micrographs show inhomogeneous contrast in the perovskite layer. Darker grains that correlate with Pb deficient areas in the elemental maps are observed. These darker grains are enriched in I and deficient in Br (see supporting information). This proofs that the aforementioned separation into I and Br rich volumes is present, although it cannot entirely be ruled out that this is an artefact due to FIB sample preparation, since this separation can be triggered by irradiation (even if no changes were observed during the STEM analysis itself). It is also found that the I-rich regions correlate with an increased concentration of Rb. For Fig. 14b and e, regions of higher Rb

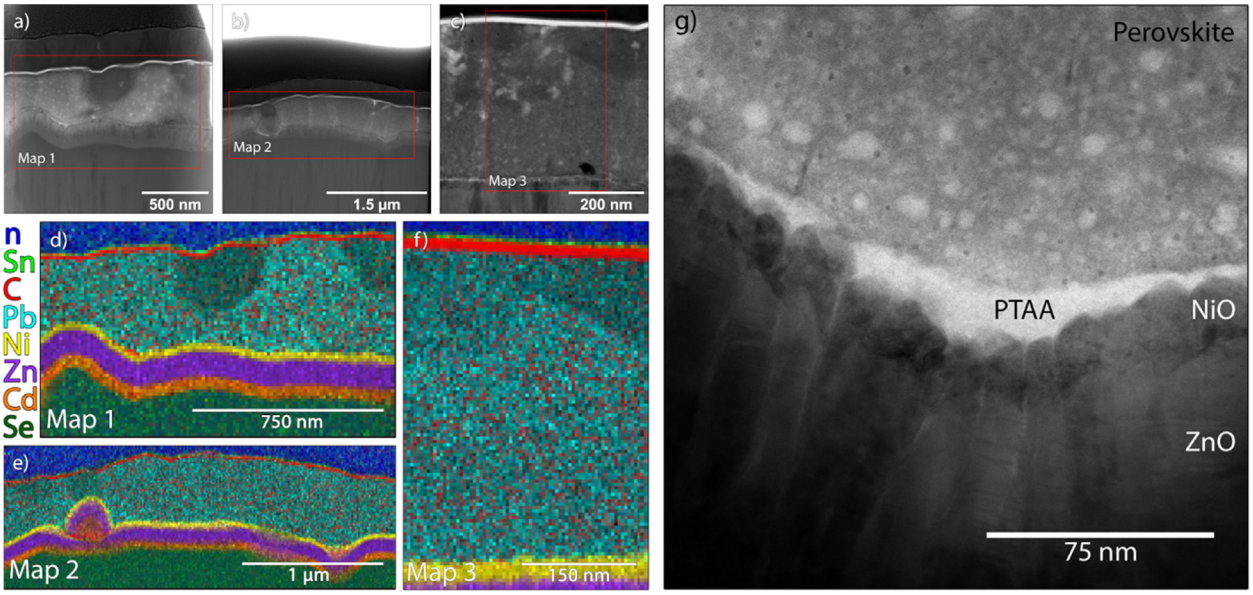

Fig 14. (a–c) TEM cross section of one of the devices. (d–f) Elemental maps of the areas in read rectangles in a–c. (g) A cross section of the interface between the perovskite, the HTL, and the mid-TCO. Noticeable are the inhomogeneities seen in the perovskite phase. Additional figures are given in the SI.

concentration are also observed, but no correlation with other elements is detected (SI). Additional contrast is observed in the perovskite layer, more clearly displayed in the STEM bright field image of higher magnification (Fig. 14g). The image was acquired in the valley of the NiO film depicted in Fig. 14a. The perovskite layer merely consists of three components, a matrix component with a uniform grey value together with brighter and darker precipitations. The brighter precipitations are non-uniform in size ranging between 2 nm and 10 nm. The darker precipitations are of uniform size and measure ca. 1.5 nm. The chemical nature of those precipitations remains unclear, but since STEM bright field images show to a high extent mass contrast, the brighter and darker contrast indicates volumes of lower and higher density, respectively. It can be assumed that the darker volumes are enriched in I and the brighter volumes are Br-rich, knowing of the chemical instability of the perovskite material. It should be pointed out, that this segregation on the nanoscale could be caused by the FIB sample preparation and could therefore be an artefact. Nevertheless, this finding shows that the instability of the perovskite structure and that irradiation might result in elemental segregation on the nanoscale.

3.7. The 2-terminal CIGS-perovskite cells. Performance and evaluation

A minimum criterion for a successful tandem device is that the resulting cell voltage is larger than that of the individual cells. According to such a definition, and if we set the threshold Voc to 1.2 V, which is higher than the highest Voc for the perovskite top-cells, a total of 116 tandem samples were produced in the project (out of 169). A more stringent requirement is that the tandem cell efficiency must be better than for the two individual cells. To compare the performance of the tandem to the top-cell is difficult as a top-cell deposited on CIGS will be different when made as a standalone unit. It is, however, reasonable to assume that tandem integrated top cells not are significantly better than their standalone counterparts which had efficiencies around 12–14% (Fig. 3b). If we count the number of tandem sample stacks that had a tandem voltage and that had a higher efficiency than both the CIGS bottom-cell and what we expect from the perovskite top-cell, the number of successful tandem sample stacks made in the project decreases to three (Fig. 15 and Table 5). A part of the reason for the low number is the non-ideal optical matching as described above (Fig. 13), but it is also a result of transmission losses in the top cell, non-ideal subcell performance, and the challenge of monolithic integration of the two cells.

One of the more interesting comparisons is to the four terminal configurations (Fig. 5). The best two-terminal devices were around 15–16% efficient, which is rather close to the 16–17% obtained for the four-terminal architecture. That means that the losses in the interconnects in the tandem stack are low. It is thus reasonable to assume that by using the procedures and the tandem stacks described here, the 2-terminal tandem performance will increase with increased performance of the sub-cells.

Combining the results discussed up to this point, we ended up with the device structure SLG/Mo/CIGS/CdS/i-ZnO/ZnO:Al/NiO/PTAA/Perovskite/LiF/PCBM/SnO_2/ITO. This device stack has most consistently given good results, both in terms of device performance and homogeneity over the sample, but some of our similar device sequences have also given good cells (as the one illustrated in Fig. 15b and c), illustrating both flexibility and room for further development. IV-data for one of the best tandem devices is given in Fig. 15d. We see a hysteresis in the IV-data that in magnitude is similar to what we see for the single junction perovskite cells. Storage in dry and dark environment for a few months did not change the JV-characteristics. If the voltage of the cell is swept multiple times in succession, the second scan have better performance, primarily as an effect of increased FF (Fig. 15e), indicating that there is a light or potential activated process that improve the current transport trough the devices. The cause of this effect is still unclear, but after the first scan the JV-characteristics stabilises at a slightly higher performance (Fig. 15e). To get an idea of the operational stability of the device, the current was measured as a function of time at a potential bias of 1.3 V, i.e. the V_{mpp} from the initial JV-scan. After a few seconds, the output efficiency stabilised at 15.0% without changing during the ten-minute measurement (Fig. 15f). For the tandem samples with this stack sequence, the homogeneity in device performance were, apart from a few edge cells, between 13 and 15.7% (Fig. 15g–j).

3.8. A note on probabilistics, and the treasure hunt character of tandem cell development

One of the challenges while developing protocols for manufacturing 2-terminal tandem devices is the sheer number of process steps and materials involved. It is enough that one of the layers in the device stack, or one of the interfaces, underperforms for the entire device to fail. In each of the processing steps, there are variations, artisanship, and hidden variables beyond our current understanding that give a non-zero probability for failure. For example, with a success rate of 98% for each layer in the device stack, the overall probability for success for an 11-layer stack is 80%. That is unacceptably low in an industrial perspective, but still rather optimistic in an exploratory research setting. This unavoidable problem leads to noise in the data and some ambiguity in the interpretation as we have seen in this work. The challenge of cell development is magnified by the problem of pinpointing the performance of one specific layer in a stack when most device characterisation techniques, e.g. JV-characteristics, primarily provide a holistic performance evaluation at the device level. Stack development thus easily ends up being a slow process hampered by limitations in the throughput rate with respect to both sample preparation capacity and cycle time from initial deposition to final cell evaluation. Ideally, one would produce hundreds of thousands of devices while systematic changing the process parameters of every single layer. Unfortunately, in most laboratories, ours included, that is far beyond the current capacity. By necessity, the development process thus gets the character of a treasure hunt, where design choices must be based on hunches and incomplete data.

We did not reach all the way towards a robust and scalable protocol for manufacturing 30% efficient CIGS-perovskite tandem devices. We do, however, hope that by sharing our data and discuss them openly where we have been successful and where we have guessed and left details for later studies, we will contribute towards mapping the vast parameter space inherent in the construction of CIGS-perovskite tandem devices which will have to be navigated to enable competitive real-world devices.

4. Conclusions

In this project, we have worked with development of 2-terminal CIGS-perovskite tandem devices. We succeeded in producing 2-terminal devices with efficiencies up to 15–16%, based on CIGS with an efficiency of around 14% and perovskites with an efficiency around 12%. The 2-terminal stack sequence that worked best in terms of efficiency and homogeneity were composed of: SLG, Mo (sputtered), CIGS (evaporated), CdS (chemical bath deposition), i-ZnO (sputtered), ZnO:Al (sputtered), NiO (sputtered), PTAA (spin-coated), perovskite (spin-coated), LiF (evaporated), PCBM (evaporated), SnO_2 (atomic layer deposition), and finally ITO (sputtered). Major obstacles to efficient device fabrication were the surface-roughness of the CIGS-stack, to obtain a uniform coverage of the layers between the CIGS and the perovskite, and to obtain a benign interface chemistry between those layers. From an optoelectronic point of view, we achieved reasonable results considering that the best 2-terminal devices in terms of efficiency only are slightly lower than the 16–17% measured in a 4-terminal configuration. By using the stack sequences and procedure described in this paper as a starting point, competitive 2-terminal devices could be developed if the

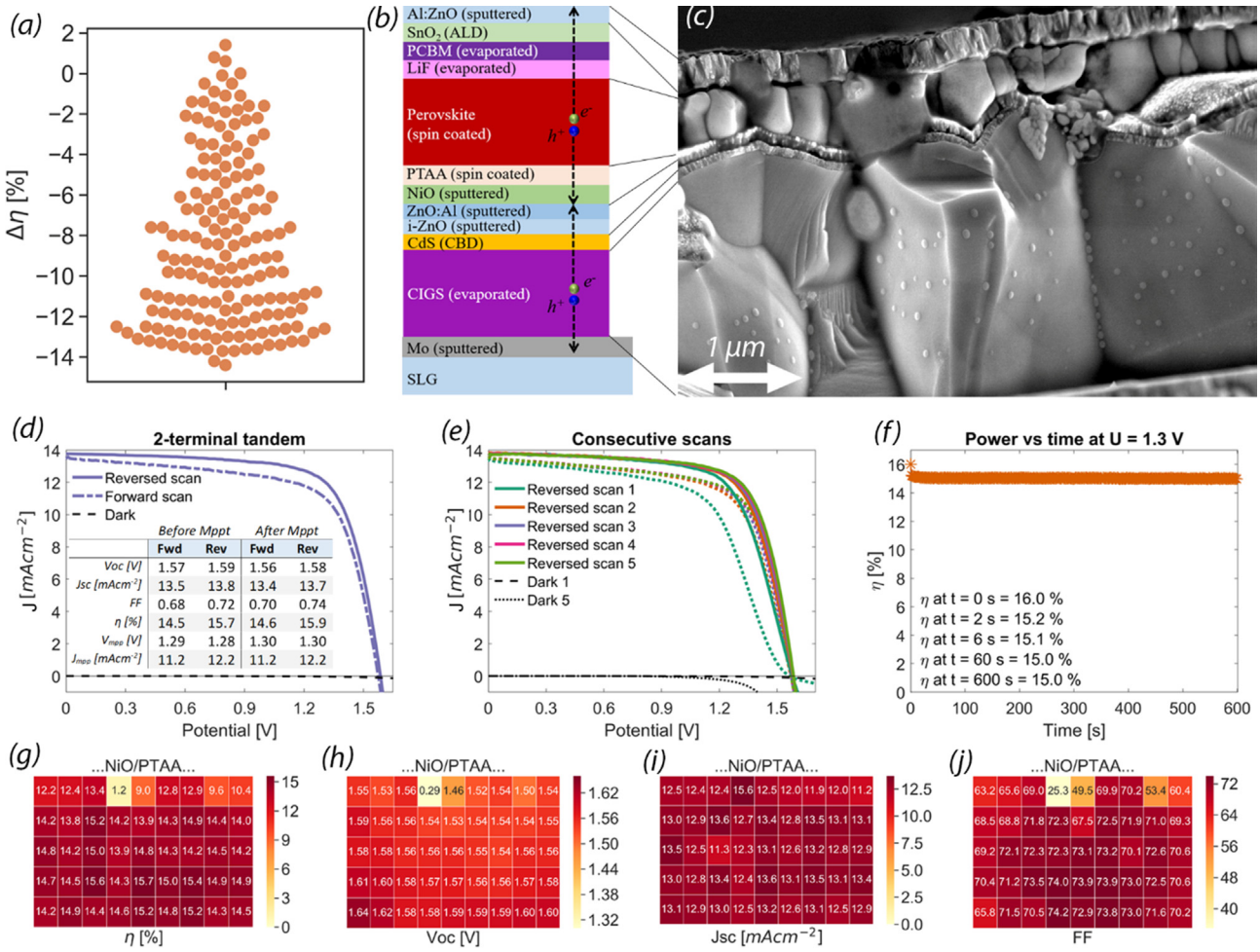

Fig. 15. (a) The difference in cell efficiency between the full tandem cell and the bottom cell defined as: $\Delta\eta = \eta_{tandem} - \eta_{bottom}$. (b) The best performing tandem stack sequence. (c) A cross section SEM image of a cell with the same stack sequence. (d) JV-characteristics for one of the best tandem cells (ID 130). (e) JV-characteristics over multiple consecutive potential scans. Dotted lines are for the reveres sweep. (f) Efficiency as a function of time for the same cell when hold at 1.3 V. (g and h) Device parameters for all cells on the substrate for one of the best samples illustrating the degree of spatial homogeneity.

Table 5
The three tandem sample stacks with a tandem voltage where the efficiency of the tandem-cell (T) where higher than that of the CIGS bottom-cell (B). For the sample with ID 66 (*), the best cell on the substrate is given, whereas for the other two cells, the values given are average values over the 45 cells on the substrates. Voc is given in in V, Jsc in mA/cm^2, PCE in %, and FF is a unitless quantity.

Cell ID	η T	η B	Voc T	Voc B	Jsc T	Jsc B	FF T	FF B
66*	15.9	14.5	1.70	0.60	14.7	32.9	0.64	0.74
130	14.1	13.3	1.56	0.56	12.8	33.2	0.70	0.72
128	13.9	13.3	1.58	0.56	13.0	33.2	0.68	0.72

optical match between the two sub cells were to be improved by further band gap engineering, and if the quality of both the CIGS and the perovskite would be improved.

Declaration of Competing Interest

The authors declare that they have no known competing financial interests or personal relationships that could have appeared to influence the work reported in this paper.

Acknowledgement

The Swedish Energy Agency (project nr 43549-1). The STandUP for Energy program. The Swedish Foundation for Strategic Research (project no. RMA15-0130)

Appendix A. Supplementary material

The full dataset for all tandem devices with stack sequence, layer information, and device performance. Experimental methods. A simple model for determining the maximum efficiency of a 2-terminal tandem cell. Additional figures concerning the perovskite baseline. The dataset with performance of the tandem devices plotted as a time series. Additional figures concerning: the CdS buffer layer, the mid TCO, the NiO HTL, the impact of PTAA, the impact of perovskite composition, the ETL, the HAXPES analysis, the top TCO, the optical matching and the band gap of the perovskites, as well as how the performance of the tandem cells compare to the bottom cells. Supplementary data to this article can be found online at https://doi.org/10.1016/j.solener.2020.06.034.

References

Abate, A., Leijtens, T., Pathak, S., Teuscher, J., Avolio, R., Errico, M.E., Kirkpatrik, J., Ball, J.M., Docampo, P., McPherson, I., Snaith, H.J., 2013. Phys. Chem. Chem. Phys. 15, 2572–2579.

Abate, A., Staff, D.R., Hollman, D.J., Snaith, H.J., Walker, A.B., 2014. Phys. Chem. Chem. Phys. 16, 1132–1138.
Albrecht, S., Saliba, M., Baena, J.P.C., Lang, F., Kegelmann, L., Mews, M., Steier, L., Abate, A., Rappich, J., Korte, L., 2016. Energ. Environ. Sci. 9, 81–88.
Almansouri, I., Ho-Baillie, A., Green, M.A., 2015. Japanese J. Appl. Phys. 54.
Almansouri, I., Ho-Baillie, A., Green, M.A., 2015. Japanese J. Appl. Phys. 54, 08KD04.
Ateto, E.O., Konagai, M., Miyajima, S., 2016. Int. J. Photoenergy 2016, 9.
Baena, J.P.C., Steier, L., Tress, W., Saliba, M., Neutzner, S., Matsui, T., Giordano, F., Jacobsson, T.J., Kandada, A.R.S., Zakeeruddin, S.M., 2015. Energ. Env. Sci. 8, 2928–2934.
Bai, Y., Xiao, S., Hu, C., Zhang, T., Meng, X., Li, Q., Yang, Y., Wong, K.S., Chen, H., Yang, S., 2017. Nano Energy 34, 58–68.
Bailie, C.D., Christoforo, M.G., Mailoa, J.P., Bowring, A.R., Unger, E.L., Nguyen, W.H., Burschka, J., Pellet, N., Lee, J.Z., Gratzel, M., Noufi, R., Buonassisi, T., Salleo, A., McGehee, M.D., 2015. Energ. Environ. Sci. 8, 956–963.
Bailie, C.D., McGehee, M.D., 2015. Mrs Bulletin 40, 681–685.
Bella, F., Renzi, P., Cavallo, C., Gerbaldi, C., 2018. Chemistry–A Eur. J. 24, 12183–12205.
Bush, K.A., Palmstrom, A.F., Zhengshan, J.Y., Boccard, M., Cheacharoen, R., Mailoa, J.P., McMeekin, D.P., Hoye, R.L., Bailie, C.D., Leijtens, T., 2017. Nat. Energ. 2, 17009.
Bush, K.A., Manzoor, S., Frohna, K., Yu, Z.J., Raiford, J.A., Palmstrom, A.F., Wang, H.-P., Prasanna, R., Bent, S.F., Holman, Z.C., 2018. ACS Energy Lett. 3, 2173–2180.
Chang, S.H., Chen, C.-C., Chen, L.-C., Tien, C.-L., Cheng, H.-M., Huang, W.-C., Lin, H.-Y., Chen, S.-H., Wu, C.-G., 2017. Sol. Energy Mater. Sol. Cells 169, 40–46.
Chen, L.-C., Chen, J.-C., Chen, C.-C., Wu, C.-G., 2015. Nanoscale Res. Lett. 10, 312.
Chen, W., Zhang, G.-N., Xu, L.-M., Gu, R., Xu, Z.-H., Wang, H.-J., He, Z.-B., 2016. Mater. Today Energy 1, 1–10.
Chen, W., Liu, F.Z., Feng, X.Y., Djurišić, A.B., Chan, W.K., He, Z.B., 2017. Adv. Enrgy. Mater. 7, 1700722.
Chouhan, A.S., Jasti, N.P., Hadke, S., Raghavan, S., Avasthi, S., 2017. Curr. Appl. Phys. 17, 1335–1340.
Ciro, J., Ramírez, D., Mejía Escobar, M.A., Montoya, J.F., Mesa, S., Betancur, R., Jaramillo, F., 2017. ACS Appl. Mater. Interfaces 9, 12348–12354.
Correa-Baena, J.-P., Abate, A., Saliba, M., Tress, W., Jesper Jacobsson, T., Gratzel, M., Hagfeldt, A., 2017. Energ. Env. Sci. 10, 710–727.
Cui, J., Meng, F., Zhang, H., Cao, K., Yuan, H., Cheng, Y., Huang, F., Wang, M., 2014. ACS Appl. Mater. Interfaces 6, 22862–22870.
de Quilettes, D.W., Vorpahl, S.M., Stranks, S.D., Nagaoka, H., Eperon, G.E., Ziffer, M.E., Snaith, H.J., Ginger, D.S., 2015. Science 348, 683–686.
Duong, T., Wu, Y., Shen, H., Peng, J., Fu, X., Jacobs, D., Wang, E.C., Kho, T.C., Fong, K.C., Stocks, M., 2017. Adv. Energy. Mater. 7, 1700228.
Edoff, M., Jarmar, T., Nilsson, N.S., Wallin, E., Högström, D., Stolt, O., Lundberg, O., Shafarman, W., Stolt, L., 2017. IEEE J. Photovolt. 7, 1789–1794.
Eperon, G.E., Leijtens, T., Bush, K.A., Prasanna, R., Green, T., Wang, J.T.-W., McMeekin, D.P., Volonakis, G., Milot, R.L., May, R., 2016. Science 354, 861–865.
Filipič, M., Löper, P., Niesen, B., De Wolf, S., Krč, J., Ballif, C., Topič, M., 2015. Optics Exp. 23, A263–A278.
Fu, F., Feurer, T., Weiss, T.P., Pisoni, S., Avancini, E., Andres, C., Buecheler, S., Tiwari, A.N., 2017. Nat. Energ. 2, 16190.
Futscher, M.H., Ehrler, B., 2017. ACS Energy Lett. 2, 2089–2095.
Giordano, F., Abate, A., Correa Baena, J.P., Saliba, M., Matsui, T., Im, S.H., Zakeeruddin, S.M., Nazeeruddin, M.K., Hagfeldt, A., Graetzel, M., 2016. Nat. Commun. 7.
Green, M.A., Dunlop, E.D., Levi, D.H., Hohl-Ebinger, J., Yoshita, M., Ho-Baillie, A.W., 2019. Progr. Photovolt.: Res. Appl. 27, 565–575.
Guchhait, A., Dewi, H.A., Leow, S.W., Wang, H., Han, G., Suhaimi, F.B., Mhaisalkar, S., Wong, L.H., Mathews, N., 2017. ACS Energy Lett. 2, 807–812.
Han, Q., Hsieh, Y.-T., Meng, L., Wu, J.-L., Sun, P., Yao, E.-P., Chang, S.-Y., Bae, S.-H., Kato, T., Bermudez, V., 2018. Science 361, 904–908.
He, J., Xiang, Y., Zhang, F., Lian, J., Hu, R., Zeng, P., Song, J., Qu, J., 2018. Nano Energy 45, 471–479.
Heo, J.H., Im, S.H., 2016. Adv. Mater. 28, 5121–5125.
Herz, L.M., 2016. Annu. Rev. Phys. Chem. 67, 65–89.
Herz, L.M., 2017. ACS Energy Lett. 2, 1539–1548.
Hörantner, M.T., Snaith, H.J., 2017. Energ. Environ. Sci. 10, 1983–1993.
Hu, C., Bai, Y., Xiao, S., Zhang, T., Meng, X., Ng, W.K., Yang, Y., Wong, K.S., Chen, H., Yang, S., 2017. J. Mater. Chem. A 5, 21858–21865.
Hultqvist, A., Platzer-Björkman, C., Zimmermann, U., Edoff, M., Törndahl, T., 2012. Progr. Photovolt.: Res. Appl. 20, 883–891.
Islam, M.B., Yanagida, M., Shirai, Y., Nabetani, Y., Miyano, K., 2017. ACS Omega 2, 2291–2299.
Jacobsson, T.J., Correa-Baena, J.-P., Halvani Anaraki, E., Philippe, B., Stranks, S.D., Bouduban, M.E.F., Tress, W., Schenk, K., Teuscher, J., Moser, J.-E., Rensmo, H., Hagfeldt, A., 2016a. J. Am. Chem. Soc. 138, 10331–10343.
Jacobsson, T.J., Correa-Baena, J.-P., Pazoki, M., Saliba, M., Schenk, K., Gratzel, M., Hagfeldt, A., 2016b. Energ. Env. Sci. 9, 1706–1724.
Jacobsson, T.J., Svanström, S., Andrei, V., Rivett, J.P., Kornienko, N., Philippe, B., Cappel, U.B., Rensmo, H.K., Deschler, F., Boschloo, G., 2018. J. Phys. Chem. C 122, 13548–13557.
Jehl, Z., Bouttemy, M., Lincot, D., Guillemoles, J., Gerard, I., Etcheberry, A., Voorwinden, G., Powalla, M., Naghavi, N., 2012. J. Appl. Phys. 111, 114509.
Jeon, N.J., Noh, J.H., Kim, Y.C., Yang, W.S., Ryu, S., Il Seol, S., 2014. Nat. Mater. 13, 897–903.
Jost, M., Bertram, T., Koushik, D., Marquez, J., Verheijen, M., Heinemann, M.D., Köhnen, E., Al-Ashouri, A., Braunger, S., Lang, F., 2019. ACS Energy Lett. 4, 583–590.
Kojima, A., Teshima, K., Shirai, Y., Miyasaka, T., 2009. J. Am. Chem. Soc. 131, 6050–6051.
Lai, W.-C., Lin, K.-W., Guo, T.-F., Lee, J., 2015. IEEE Trans. Electron Dev. 62, 1590–1595.
Lany, S., Zunger, A., 2006. J. Appl. Phys. 100, 113725.
Lee, T.D., Ebong, A.U., 2017. Renew. Sust. Energ. Rev. 70, 1286–1297.
Li, G., Jiang, Y., Deng, S., Tam, A., Xu, P., Wong, M., Kwok, H.S., 2017. Adv. Sci. 4, 1700463.
Li, Y.-F., Selloni, A., 2014. ACS Catal. 4, 1148–1153.
Lindahl, J., Zimmermann, U., Szaniawski, P., Törndahl, T., Hultqvist, A., Salomé, P., Platzer-Björkman, C., Edoff, M., 2013. IEEE J. Photovolt. 3, 1100–1105.
Mailoa, J.P., Bailie, C.D., Johlin, E.C., Hoke, E.T., Akey, A.J., Nguyen, W.H., McGehee, M.D., Buonassisi, T., 2015. Appl. Phys. Lett. 106, 121105.
Mudryi, A., Gremenok, V., Karotki, A., Zalesski, V., Yakushev, M., Luckert, F., Martin, R., 2010. J. App. Spectrosc. 77, 371–377.
Nie, W., Tsai, H., Blancon, J.C., Liu, F., Stoumpos, C.C., Traore, B., Kepenekian, M., Durand, O., Katan, C., Tretiak, S., 2018. Adv. Mater. 30, 1703879.
Pae, S.R., Byun, S., Kim, J., Kim, M., Gereige, I., Shin, B., 2017. ACS Appl. Mater. Interfaces 10, 534–540.
Park, N.G., Gratzel, M., Miyasaka, T., Zhu, K., Emery, K., 2016. Nat. Energ. 1, 8.
Park, I.J., Kang, G., Park, M.A., Kim, J.S., Seo, S.W., Kim, D.H., Zhu, K., Park, T., Kim, J.Y., 2017. ChemSusChem 10, 2660–2667.
Park, J.H., Seo, J., Park, S., Shin, S.S., Kim, Y.C., Jeon, N.J., Shin, H.W., Ahn, T.K., Noh, J.H., Yoon, S.C., 2015. Adv. Mater. 27, 4013–4019.
Qin, P., Tanaka, S., Ito, S., Tetreault, N., Manabe, K., Nishino, H., Nazeeruddin, M.K., Grätzel, M., 2014. Nat. Commun. 5.
Quiroz, C.O.R., Shen, Y., Salvador, M., Forberich, K., Schrenker, N., Spyropoulos, G.D., Heumüller, T., Wilkinson, B., Kirchartz, T., Spiecker, E., 2018. J. Mater. Chem. A 6, 3583–3592.
Raja, W., Schmid, M., Toma, A., Wang, H., Alabastri, A., Proietti Zaccaria, R., 2017. ACS Photonics 4, 2025–2035.
Rajagopal, A., Yang, Z., Jo, S.B., Braly, I.L., Liang, P.W., Hillhouse, H.W., Jen, A.K.Y., 2017. Adv. Energy Mater. 29, 1702140.
Rao, H., Ye, S., Sun, W., Yan, W., Li, Y., Peng, H., Liu, Z., Bian, Z., Li, Y., Huang, C., 2016. Nano Energy 27, 51–57.
Rühle, S., 2016. Sol. Energ. 130, 139–147.
Sahli, F., Werner, J., Kamino, B.A., Bräuninger, M., Monnard, R., Paviet-Salomon, B., Barraud, L., Ding, L., Leon, J.J.D., Sacchetto, D., 2018a. Nat. Mater. 17, 820.
Sahli, F., Werner, J., Kamino, B.A., Brauninger, M., Monnard, R., Paviet-Salomon, B., Barraud, L., Ding, L., Diaz Leon, J.J., Sacchetto, D., Cattaneo, G., Despeisse, M., Boccard, M., Nicolay, S., Jeangros, Q., Niesen, B., Ballif, C., 2018b. Nat. Mater. 17, 820–826.
Saliba, M., 2019. Adv. Enrgy. Mater. 1803754.
Saliba, M., Matsui, T., Seo, J.Y., Domanski, K., Correa-Baena, J.P., Nazeeruddin, M.K., Zakeeruddin, S.M., Tress, W., Abate, A., Hagfeldt, A., Gratzel, M., 2016a. Energ. Env. Sci. 9, 1989–1997.
Saliba, M., Matsui, T., Domanski, K., Seo, J.Y., Ummadisingu, A., Zakeeruddin, S.M., Correa-Baena, J.P., Tress, W.R., Abate, A., Hagfeldt, A., Gratzel, M., 2016b. Science 354, 206–209.
Saliba, M., Correa-Baena, J.-P., Wolff, C.M., Stolterfoht, M., Phung, N., Albrecht, S., Neher, D., Abate, A., 2018a. Chem. Mater. 30, 4193–4201.
Saliba, M., Correa-Baena, J.P., Gratzel, M., Hagfeldt, A., Abate, A., 2018b. Angew. Chem. Int. Ed. Engl. 57, 2554–2569.
Seo, J., Park, S., Kim, Y.C., Jeon, N.J., Noh, J.H., Yoon, S.C., Seok, S.I., 2014a. Energ. Env. Sci. 7, 2642–2646.
Seo, J., Park, S., Chan Kim, Y., Jeon, N.J., Noh, J.H., Yoon, S.C., Seok, S.I., 2014b. Energ. Env. Sci. 7, 2642–2646.
Seo, S., Park, I.J., Kim, M., Lee, S., Bae, C., Jung, H.S., Park, N.-G., Kim, J.Y., Shin, H., 2016. Nanoscale 8, 11403–11412.
Shen, H.P., Duong, T., Peng, J., Jacobs, D., Wu, N.D., Gong, J.B., Wu, Y.L., Karuturi, S.K., Fu, X., Weber, K., Xiao, X.D., White, P., Catchpolea, K., 2018. Energ. Environ. Sci. 11, 394–406.
Sheng, R., Horantner, M.T., Wang, Z., Jiang, Y., Zhang, W., Agosti, A., Huang, S., Hao, X., Ho-Baillie, A., Green, M., Snaith, H.J., 2017. J. Phys. Chem. C 121, 27256–27262.
Shockley, W., Queisser, H., 1961. J. Appl. Phys. 32, 510–519.
Siebentritt, S., Igalson, M., Persson, C., Lany, S., 2010. Progr. Photovolt.: Res. Appl. 18, 390–410.
Stolterfoht, M., Wolff, C.M., Márquez, J.A., Zhang, S., Hages, C.J., Rothhardt, D., Albrecht, S., Burn, P.L., Meredith, P., Unold, T., 2018. Nat. Energ. 3, 847.
Stranks, S.D., Eperon, G.E., Grancini, G., Menelaou, C., Alcocer, M.J., Leijtens, T., Herz, L.M., Petrozza, A., Snaith, H.J., 2013. Science 342, 341–344.
Sun, W., Ye, S., Rao, H., Li, Y., Liu, Z., Xiao, L., Chen, Z., Bian, Z., Huang, C., 2016. Nanoscale 8, 15954–15960.
Unger, E., Kegelmann, L., Suchan, K., Sörell, D., Korte, L., Albrecht, S., 2017. J. Mater. Chem. A 5, 11401–11409.
Van der Ven, A., Morgan, D., Meng, Y., Ceder, G., 2006. J. Electrochem. Soc. 153, A210–A215.
Wei, H., Shi, J., Xu, X., Xiao, J., Luo, J., Dong, J., Lv, S., Zhu, L., Wu, H., Li, D., 2015. Phys. Chem. Chem. Phys. 17, 4937–4944.
Wei, Y., Yao, K., Wang, X., Jiang, Y., Liu, X., Zhou, N., Li, F., 2018. Appl. Surf. Sci. 427, 782–790.
Werner, J., Sahli, F., Fu, F., Diaz Leon, J.J., Walter, A., Kamino, B.A., Niesen, B., Nicolay, S., Jeangros, Q., Ballif, C., 2018a. ACS Energy Lett. 3, 2052–2058.
Werner, J., Niesen, B., Ballif, C., 2018b. Adv. Mater. Inter. 5, 1700731.
Wu, Y., Xie, F., Chen, H., Yang, X., Su, H., Cai, M., Zhou, Z., Noda, T., Han, L., 2017. Adv. Mater. 29, 1701073.
Xiao, M., Huang, F., Huang, W., Dkhissi, Y., Zhu, Y., Etheridge, J., Gray-Weale, A., Bach, U., Cheng, Y.-B., Spiccia, L., 2014. Angew. Chem. Int. Edit. 53, 9898–9903.
Xiao, S., Xu, F., Bai, Y., Xiao, J., Zhang, T., Hu, C., Meng, X., Tan, H., Ho, H.P., Yang, S., 2019. Solar RRL 3, 1800278.

Xie, F., Chen, C.-C., Wu, Y., Li, X., Cai, M., Liu, X., Yang, X., Han, L., 2017. Energ. Env. Sci. 10, 1942–1949.
Xue, Q., Bai, Y., Liu, M., Xia, R., Hu, Z., Chen, Z., Jiang, X.F., Huang, F., Yang, S., Matsuo, Y., 2017. Adv. Enrgy. Mater. 7, 1602333.
Yang, Y.M., Chen, Q., Hsieh, Y.T., Song, T.B., Marco, N.D., Zhou, H., Yang, Y., 2015. ACS Nano 9, 7714–7721.
Ye, S., Sun, W., Li, Y., Yan, W., Peng, H., Bian, Z., Liu, Z., Huang, C., 2015. Nano Lett. 15, 3723–3728.
Yin, W.-J., Shi, T., Yan, Y., 2014. Appl. Phys. Lett. 104, 063903.
Yu, Z.S.J., Carpenter, J.V., Holman, Z.C., 2018. Nat. Energ. 3, 747–753.
Zhao, Y., Zhu, K., 2014. J. Phys. Chem. Lett 5, 4175–4186.
Zheng, J., Lau, C.F.J., Mehrvarz, H., Ma, F.-J., Jiang, Y., Deng, X., Soeriyadi, A., Kim, J., Zhang, M., Hu, L.J.E., 2018. Energ. Environ. Sci. 11, 2432–2443.
Zhou, L., Chang, J., Liu, Z., Sun, X., Lin, Z., Chen, D., Zhang, C., Zhang, J., Hao, Y., 2018. Nanoscale 10, 3053–3059.
Zhou, Y., Zhao, Y., 2019. Energ. Env. Sci. 12, 1495–1511.